Axial-azimuthal, high-frequency modes from global linear-stability model of a Hall thruster

Axial-azimuthal, high-frequency modes from global linear-stability model of a Hall thruster

Enrique Bello-Benítez* and Eduardo Ahedo†
Universidad Carlos III de Madrid, Leganés, Spain

December 24, 2020

Abstract

Axial-azimuthal instabilities of a Hall-thruster plasma discharge are investigated using fluid model and a linear global stability approach, appropriate to the large axial inhomogeneity of the equilibrium solution. Electron pressure and electron inertia are considered in both the equilibrium and perturbed solutions. Fourier transform in time and azimuth are taken and the dispersion relation for the resultant Sturm-Liouville problem governing the axial behavior of the modes is numerically obtained. The analysis, focused in mid-to-high frequencies and large wavenumbers identifies two main instability types. The dominant mode develops in the near plume at 1-5 MHz and azimuthal mode numbers $\sim$ 10-50, has a weak ion response and seems to be triggered by negative gradients of the magnetic field. The subdominant mode develops near the anode at 100-300 kHz and azimuthal mode numbers $\sim$ 1-10, and seems of the rotating-spoke type. Both instabilities are well characterized by investigating their oblique propagation, the influence of design and operation parameters, and the effects of anode-cathode electric connection, electron inertia, and temperature perturbations. The possible impact of these instabilities on electron cross-field transport is estimated through a quasilinear approach, which yields a spatially-rippled turbulent force.

1 Introduction

Instabilities and their role in electron cross-field transport is the main open problem in Hall-effect thruster (HET) discharges. Although oscillations modes within a large range of frequencies and wavevectors have been observed in experiments and simulations [1] there is not yet a fully established classification and characterization of them. Among all oscillation modes, azimuthal ones are potential candidates to contribute to cross-field transport through, at least, a net azimuthal electric force coming from correlated oscillations of plasma density and azimuthal electric field [2, 3].

Among the different lines of research, linear stability analyses provide the basic stage in order to identify the instability modes and characterizing them physically. Linear stability studies can be based on either kinetic or fluid formulations, and they can be local (generally limited to a given axial section of the HET discharge) or global (dealing with the whole extension of the discharge). Kinetically based studies are generally local, due to their high complexity, and, in the context of HET plasmas, lead to dispersion relations for the electron-cyclotron drift instability [4, 5, 6, 7] and the modified two-stream instability

*PhD. Student, ebello@ing.uc3m.es, Equipo de Propulsión Espacial y Plasmas (EP2)
†Professor, eduardo.ahedo@uc3m.es, EP2

[8, 9, 10]. Fluid formulations are amenable to local and global studies and the modal families resulting are quite diverse. Global analyses, which take into account the large inhomogeneity of the plasma discharge, are more consistent and localize the regions where instabilities develop.

A stationary axial model of the inhomogeneous HET discharge [11, 12] was used by Escobar and Ahedo to carry out linear global stability studies at both low-frequencies (the 10-100 Khz range, say) and high-frequencies (the 1-10 MHz range, say), with azimuthal wavemodes of order unity[13, 14]. The papers included an extensive literature review on the subject, that we, thus, omit here. The low-frequency global analysis [13] was quite extensive: equilibrium and perturbation models kept all relevant terms, the central role of ionization instabilities was highlighted, as well as the relation with experimental evidence, and the comparison with a previous local analysis [15] was made.

The high-frequency global analysis [14], centered in the MHz range, was more limited in scope. First, several simplifications were applied to the perturbation model in order to recover the global dispersion relations of previous studies on Rayleigh and lower-hybrid instabilities by Litvak and Fisch [16] and Kapulkin et al. [17, 18]. Second, the analysis was limited to low azimuthal mode numbers. And third, electron pressure was ignored, which is now believed an important shortcoming inside the HET chamber. More recently, Sorokina et al. [19] discussed the existence of drift-gradient, near-anode modes using typical plasma-parameter profiles and a global dispersion relation that coincides with the collisionless limit of reference [14] except for the treatment of the compressibility of the electron velocity field; both models ignore the electron pressure. Marusov et al. [20] apply the same logic than references [14] and [19] to a magnetron-type geometry with a constant magnetic field. Romadanov et al. [21] have also discussed a global perturbation model aiming at the regimes of drift-gradient and lower-hybrid instabilities [22, 23]. The model has the peculiarity of being applied to a fully empirical equilibrium solution, where 7/8 of the domain corresponds to the external plume, and, similarly to Refs. [14, 19, 20], the perturbation problem is simplified into a second-order differential equation for the electric potential perturbation.

The present work analyzes global fluid instabilities of the inhomogeneous HET discharge in the mid-to-high ranges of both frequency and azimuthal wavenumber, but always respecting the limits of validity of the multi-fluid formulation, i.e. frequencies and wavenumbers much smaller, respectively, than the electron gyrofrequency and the inverse of the electron gyroradius. Compared to the previously mentioned global analyses, the axial-azimuthal model considered here keeps fully the effects of: (i) the electron pressure, in order to cover both the subsonic and supersonic regions of the discharge; and (ii) the electron inertia, in order to assess their relevance in equilibrium and perturbation solutions, and turbulence-based forces. In references [14, 21, 19, 20], electron inertia was included directly as a small correction to the leading $E \times B$ drift velocity in the final mathematical model.

Several studies with nonlinear particle-in-cell simulations are proposing the turbulent electric force generated by electron-drift kinetic instabilities as the main driver of the anomalous cross-field transport of electrons in HET discharges [24, 3, 25, 7, 26]. The fluid instabilities discussed here develop in a frequency range not far from the above kinetic ones. This has motivated us to consider the quasilinear extension of the global fluid model, based on estimating the quadratically correlated terms in the electron momentum equation, in order to speculate on the possible contribution to anomalous transport of the electric and inertia forces generated by those fluid instabilities.

The zeroth and first-order formulations of the axial-azimuthal model, and the equilibrium solution are presented in Sec. 2. The fluid model assumes quasineutrality except at the anode sheath. The inclusion of electron azimuthal inertia in the equilibrium solution is rather novel. Since the low frequency range is out of the scope here, neutral dynamics are disregarded in the first-order problem.

Sections 3 and 4 analyze the eigenvalues and eigenmodes of the global dispersion relation of a 'nominal model', with no electron inertia effects in equilibrium and no temperature perturbations. This case is very comparable with the majority of local analyses in the literature [27, 23, 28] and shows a manageable number of unstable branches. A dominant near-plume and a subdominant near-anode instabilities are identified. The quasineutrality and axial-wavenumber spectrum of these instabilities are checked, and an investigation of design and operation parameters is conducted in order to assure the robustness of the characterization of these instabilities.

Section 5 investigates how the dispersion relation and the resulting eigenmodes are modified in 'off-nominal models', in particular when zeroth-order electron inertia is included or when electron temperature perturbations are allowed. Section 6 analyzes the dominant perturbation forces in the electron momentum equation and attempts to estimate the relevance of the instabilities studied here in the electron cross-field transport.

2 Model Formulation

A time-dependent, axial-azimuthal, fluid model of a Hall thruster is considered. Since the radial direction is excluded, plasma magnitudes will be in fact radially-averaged values, while the plasma interaction with radial walls is included as source terms in the axial-azimuthal model. In particular, for a generic vector variable $\boldsymbol{v}(z, y, t)$, its divergence will be expressed as

$$\nabla \cdot \boldsymbol{v} = \hat{\nabla} \cdot \boldsymbol{v} + v'_w, \qquad \hat{\nabla} \cdot \boldsymbol{v} = \frac{\partial v_y}{\partial y} + \frac{1}{A_c}\frac{\partial}{\partial z}\left(A_c v_z\right), \tag{1}$$

where: $y = R\theta$ is the azimuthal arc (with R the annular channel mid-radius), z is the axial coordinate, A_c is the cross-sectional area of the plasma beam, and v'_w is the radial wall contribution to magnitude $\boldsymbol{v}(z, y, t)$. As sketched in figure 1, the plasma domain goes from the anode A (at $z = 0$) to the chamber exit E (at $z = L_\mathrm{E}$) and the external cathode (at $z = L_\mathrm{N}$), which is treated here as an infinitely-thin source of electrons. This assumption decouples the current-free region downstream of the plume, which is here left out of the analysis. Since the radial direction is omitted, the plasma is quasineutral everywhere except at the infinitely-thin Debye sheath next to the anode, B being the sheath edge in figure 1.

The plasma is constituted of neutrals, singly-charged ions and electrons, with subscripts n, i, and e, respectively. The equations for the quasineutral plasma are based in previous works by Ahedo and co-workers [11]. Using conventional notation, they are the following:

$$\frac{\partial n_n}{\partial t} + \hat{\nabla} \cdot (n_n \boldsymbol{u}_n) = -n(\nu_p - \nu_w), \tag{2}$$

$$\frac{\partial n}{\partial t} + \hat{\nabla} \cdot (n \boldsymbol{u}_i) = n(\nu_p - \nu_w), \tag{3}$$

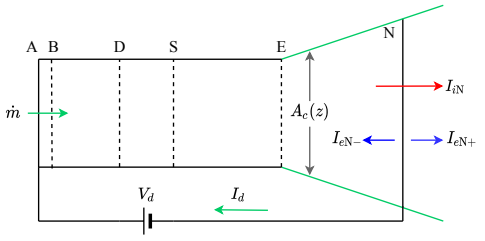

Figure 1: Schematic representation of the plasma discharge in a Hall thruster. $\dot{m}$ is the mass flow, V_d is the discharge voltage, I_d the discharge current, and $I_{i\mathrm{N}}$ is the ion current flowing downstream. The electron current flowing from anode A to neutralizer N, $-I_d$, splits into the downstream neutralizing current, $I_{\mathbf{N}+} = I_{i\mathbf{N}}$, and the upstream ionizing current $I_{e\mathrm{N}-} = I_d - I_{i\mathrm{N}}$. E is the chamber exit, B is the anode sheath edge, D is the ion stagnation point, and S is the ion sonic point. $A_c(z)$ is the effective cross-section area.

$$\frac{\partial n}{\partial t} + \hat{\nabla} \cdot (n\boldsymbol{u}_e) = n(\nu_p - \nu_w), \tag{4}$$

$$m_i n_n \left(\frac{\partial \boldsymbol{u}_n}{\partial t} + \boldsymbol{u}_n \cdot \nabla \boldsymbol{u}_n \right) = m_i n [\nu_w (\boldsymbol{u}_{nw} - \boldsymbol{u}_n) + \nu_{in} (\boldsymbol{u}_i - \boldsymbol{u}_n)] \tag{5}$$

$$m_i n \left(\frac{\partial \boldsymbol{u}_i}{\partial t} + \boldsymbol{u}_i \cdot \nabla \boldsymbol{u}_i \right) = -en\nabla\phi + m_i n \nu_i (\boldsymbol{u}_n - \boldsymbol{u}_i), \tag{6}$$

$$m_e n \left(\frac{\partial \boldsymbol{u}_e}{\partial t} + \boldsymbol{u}_e \cdot \nabla \boldsymbol{u}_e \right) = -\nabla (nT_e) + en (\nabla\phi - \boldsymbol{u}_e \times \boldsymbol{B}) - m_e n \nu_e \boldsymbol{u}_e, \tag{7}$$

$$\frac{\partial}{\partial t} \left(\frac{3}{2} n T_e \right) + \hat{\nabla} \cdot \left(\frac{5}{2} n T_e \boldsymbol{u}_e + \boldsymbol{q}_e \right) = \boldsymbol{u}_e \cdot \nabla (nT_e) - n\nu_p E_{\mathrm{inel}} - n\nu_{we} T_e + m_e n \nu_e u_e^2, \tag{8}$$

$$0 = \frac{5}{2} n T_e \nabla T_e + e\boldsymbol{q}_e \times \boldsymbol{B} + m_e \nu_e \boldsymbol{q}_e. \tag{9}$$

In equations (2)-(4): ν_p is the plasma production (i.e., ionization) frequency, and $n\nu_w$ is the source term for particle losses at radial walls. Equations (5)-(7) are a combination of the corresponding species momentum and particle conservation equations. In equation (5): $\boldsymbol{u}_{nw}$ is the effective neutral velocity from plasma recombination at lateral walls, ν_{in} is the frequency of charge-exchange collisions, and neutral pressure has been neglected. In equation (6): ϕ is the electrostatic potential, ion pressure and magnetization have been neglected, and $\nu_i = \nu_{in} + \nu_p$ is the total collision frequency for ions. In equation (7): $\boldsymbol{B}$ is the applied magnetic field and

$$\nu_e = \nu_{en} + \nu_{ei} + \nu_{wm} + \nu_t \tag{10}$$

is an effective collision frequency for electrons, which includes contributions from electron-neutral collisions (ν_{en}), electron-ion collisions (ν_{ei}), effective wall-collisionality (ν_{wm}), and turbulent transport (ν_t). In equation (8): E_{inel} is the effective ionization-plus-excitation

energy cost per ionization event, and $n\nu_{we}T_e$ accounts for energy losses at lateral walls. Appendix A compiles the auxiliary models for all the collisionality terms included in the model. The effective cross-section area of the beam, A_c, is taken constant inside the channel and follows $\mathrm{d}A_c/\mathrm{d}z = 4\pi R(T_{eE}/m_i)^{1/2}/u_{zi}$ in the plume.

Azimuthal fluxes are considered relevant only for electrons, so that

$$\boldsymbol{u}_n = u_{zn}\mathbf{1}_z, \quad \boldsymbol{u}_i = u_{zi}\mathbf{1}_z, \quad \boldsymbol{u}_e = u_{ye}\mathbf{1}_y + u_{ze}\mathbf{1}_z,$$

and the electron heat flux is $\boldsymbol{q}_e = q_{ye}\mathbf{1}_y + q_{ze}\mathbf{1}_z$. The magnetic field is approximated as

$$\boldsymbol{B}(z) = \mathbf{1}_r \; B_m \exp\left[-\frac{(z-z_m)^2}{L_m^2}\right], \tag{11}$$

where z_m (generally at the thruster exit $z_m = L_\mathrm{E}$) is the location of the maximum field B_m, and L_m determines the rate of decay of the magnetic field in the thruster, which is generally different inside ($L_{m,\mathrm{in}}$) and outside ($L_{m,\mathrm{out}}$) the thruster.

Axial-azimuthal oscillatory modes in a Hall thruster discharge are studied as small perturbations of the axisymmetric equilibrium solution of the above model. Under this approach, the plasma variables are expressed as

$$\varphi(y,z,t) = \varphi_0(z) + \tilde{\varphi}_1(y,z,t), \tag{12}$$

where φ represents every plasma variable, φ_0 is the equilibrium part and $\tilde{\varphi}_1$ is the perturbation part, satisfying $|\tilde{\varphi}_1| \ll |\varphi_0|$. When expanding equations (2)-(8) in this way, the leading (or zeroth) order yields a system of ordinary differential equations that determines the axial equilibrium solution. The next order yields the set of linear perturbation equations with axially-varying coefficients, which depend on the equilibrium solution. Since the equilibrium solution is azimuthally homogeneous, the Fourier transform in both t and y of the perturbation equations can be taken, which is equivalent to write every first-order variable as

$$\tilde{\varphi}_1(z,y,t) = \mathrm{Re}\{\varphi_1(z,k_y,\omega)\exp\left(-\mathrm{i}\omega t + \mathrm{i}k_y y\right)\}, \tag{13}$$

where k_y is the real azimuthal wavenumber, $\omega = \omega_r + \mathrm{i}\gamma$ is the complex (angular) frequency, and $\varphi_1(z,k_y,\omega)$ is the complex amplitude of the perturbations, which keeps the axial dependence. Formally, due to azimuthal periodicity only integer mode numbers $k_y R$ can exist, but this restriction will add nothing relevant to the analysis hereafter.

2.1 Equilibrium solution

The stationary ($\partial/\partial t = 0$) axisymmetric ($\partial/\partial y = 0$) form of the set of equations (2)-(8), governing the plasma equilibrium solution, reads

$$-\frac{\mathrm{d}}{\mathrm{d}z}\left(A_c n_{n0} u_{zn0}\right) = \frac{\mathrm{d}}{\mathrm{d}z}\left(A_c n_0 u_{zi0}\right) = \frac{d}{dz}\left(A_c n_0 u_{ze0}\right) = A_c n_0\left(\nu_p - \nu_w\right), \tag{14}$$

$$m_i n_{n0} u_{zn0}\frac{\mathrm{d}u_{zn0}}{\mathrm{d}z} = m_i n_0\left[\nu_w\left(u_{znw} - u_{zn0}\right) + \nu_{in}\left(u_{zi0} - u_{zn0}\right)\right], \tag{15}$$

$$m_i n_0 u_{zi0}\frac{\mathrm{d}u_{zi0}}{\mathrm{d}z} = -e n_0\frac{\mathrm{d}\phi_0}{\mathrm{d}z} + m_i n_0 \nu_i\left(u_{zn0} - u_{zi0}\right), \tag{16}$$

$$0 = -\frac{\mathrm{d}}{\mathrm{d}z}\left(n_0 T_{e0}\right) + e n_0 \frac{\mathrm{d}\phi_0}{\mathrm{d}z} + e n_0 u_{ye0} B - m_e n_0 \nu_e u_{ze0}, \tag{17}$$

$$m_e n_0 u_{ze0} \frac{\mathrm{d}u_{ye0}}{\mathrm{d}z} = -e n_0 u_{ze0} B - m_e n_0 \nu_e u_{ye0}, \tag{18}$$

$$\frac{\mathrm{d}}{\mathrm{d}z}\left(\frac{5}{2} n_0 T_{e0} u_{ze0} + q_{ze0}\right) = u_{ze0} \frac{\mathrm{d}}{\mathrm{d}z}\left(n_0 T_{e0}\right) - n_0 \nu_p E_{\mathrm{inel}} - n_0 \nu_{we} T_{e0} + m_e n_0 \nu_e u_{e0}^2 - \left(\frac{5}{2} n_0 T_{e0} u_{ze0} + q_{ze0}\right) \frac{\mathrm{d}\ln A_c}{\mathrm{d}z}, \tag{19}$$

$$q_{ze0} = -\frac{5 n_0 T_{e0}}{2 m_e} \frac{\nu_e}{\nu_e^2 + \omega_{ce}^2} \frac{\mathrm{d}T_{e0}}{\mathrm{d}z}. \tag{20}$$

In equation (17), axial electron inertia has been discarded since it is always negligible. However, azimuthal electron inertia can be relevant and has been kept in equation (18). In equation (20), $\omega_{ce} = eB/m_e$ stands for the electron gyrofrequency and the azimuthal heat flow equation has been used in order to eliminate q_{ye0} from the system. The continuity equations (14) can be combined by pairs and integrated to yield

$$A_c m_i \left(n_{n0} u_{zn0} + n_0 u_{zi0}\right) = \mathrm{const} = \dot{m}, \tag{21}$$

$$A_c e n_0 \left(u_{zi0} - u_{ze0}\right) = \mathrm{const} = I_d, \tag{22}$$

being $\dot{m}$ and I_d, the total mass flow and the electric current flowing between anode and cathode, respectively. The discharge current is also the current flowing through the external anode-cathode circuit, since the plume downstream of point N is assumed current-free.

The rearrangement of the above ordinary differential problem, shows the possible existence of singularities at sonic points, defined by $u_{zi0} = \pm c_{s0}$, with $c_{s0} = \sqrt{T_{e0}/m_i}$. For instance, the equation for the derivative of the ion velocity reads

$$\left(T_{e0} - m_i u_{zi0}^2\right) \frac{\mathrm{d}u_{zi0}}{\mathrm{d}z} = G_0, \tag{23}$$

with

$$G_0 = T_{e0}\left(\nu_p - \nu_w\right) - u_{zi0} T_{e0} \frac{\mathrm{d}\ln A_c}{\mathrm{d}z} - e B u_{zi0} u_{ye0} + m_i \nu_i u_{zi0}\left(u_{zi0} - u_{zn0}\right) - \frac{2 m_e}{5 n_0 T_{e0}} \frac{\nu_e^2 + \omega_{ce}^2}{\nu_e} u_{zi0} q_{ze0}. \tag{24}$$

The axial boundary conditions for the equilibrium problem are the following.

1. The total mass flow $\dot{m}$ injected at the anode is known.
2. The injection velocity of neutrals at the anode $u_{zn0\mathrm{A}}$ is known and the sheath is transparent for neutrals.
3. The ion velocity is backwards and sonic at the anode sheath edge, $u_{zi0\mathrm{B}} = -c_{s0\mathrm{B}}$.
4. The electric potential is set zero at the cathode, $\phi_{\mathrm{N}} = 0$.

5. Taking then $\phi_{0\mathrm{A}} = V_d$, the electric potential at the anode sheath edge is

$$\phi_{0\mathrm{B}} = V_d + \phi_{0\mathrm{AB}}, \quad \phi_{0\mathrm{AB}} = \frac{T_{e0\mathrm{B}}}{e} \ln \frac{\bar{c}_{e0\mathrm{B}}}{4|u_{ze0\mathrm{B}}|}, \tag{25}$$

   where $\bar{c}_e = \sqrt{8T_e/\pi m_e}$ is the electron thermal velocity.

6. The heat flux at the anode sheath edge is [29]

$$q_{ze0\mathrm{B}} = n_{0\mathrm{B}} u_{ze0\mathrm{B}} \left(e\phi_{0\mathrm{AB}} - \frac{1}{2} T_{0e\mathrm{B}} \right). \tag{26}$$

7. There is a regular forward sonic transition inside the channel, at an unknown location S, satisfying

$$u_{zi0\mathrm{S}} = c_{s0\mathrm{S}}, \qquad G_{0\mathrm{S}} = 0. \tag{27}$$

8. The temperature of injected electrons at the cathode N, $T_{e0\mathrm{N}}$, is known.

9. The electrons are emitted at N with null azimuthal velocity, i.e. $u_{ye0\mathrm{N}} = 0$.

Since V_d is an input, the discharge current I_d is an output. The opposite choice is valid too. The circuit boundary condition does not change the equilibrium solution but it does on the perturbation modes, as it will be shown later.

Table 1: Nominal simulation case parameters, based on a SPT-100-type Hall thruster, used in this work and defined in the main text. $A_{c,\mathrm{in}}$ is the chamber cross-section area.

$\dot{m}$	4.75 mg s^{-1}	V_d	300 V
B_m	251 G	z_m	2.5 cm
L_E	2.5 cm	L_N	3.35 cm
$A_{c,\mathrm{in}}$	40 cm^2	R	4.25 cm
$T_{e\mathrm{N}}$	5 eV	$u_{zn\mathrm{B}}$	300 m s^{-1}
$L_{m,\mathrm{in}}$	1.5 cm	$L_{m,\mathrm{out}}$	0.5 cm

The parameters of the nominal simulation case, based on previous works [13, 14], are gathered in table 1. The resulting stationary solution is plotted in figure 2. The main features of this solution were thoroughly discussed in [30, 29, 11]. The only interesting novelty here is the inclusion of azimuthal electron inertia. This is motivated by consistency, since electron azimuthal inertia is known to be important in high-frequency, short wavelength perturbation modes, such as lower-hybrid oscillations [31, 23]. To assess the relevance of electron azimuthal inertia in the stationary solution, figure 2 plots the solution for two different models. First, there is Model 0A excluding the azimuthal electron inertia, when the electron azimuthal momentum equation (18) reduces to the algebraic relation

$$u_{ye0} = -\frac{\omega_{ce}}{\nu_e} u_{ze0}, \tag{28}$$

(and the ninth boundary condition above is not applied). Then, there is Model 0B, which includes the electron azimuthal inertia term. The comparison of Models 0A and 0B shows that, in Model 0B, unmagnetized electrons emitted from the cathode with zero azimuthal

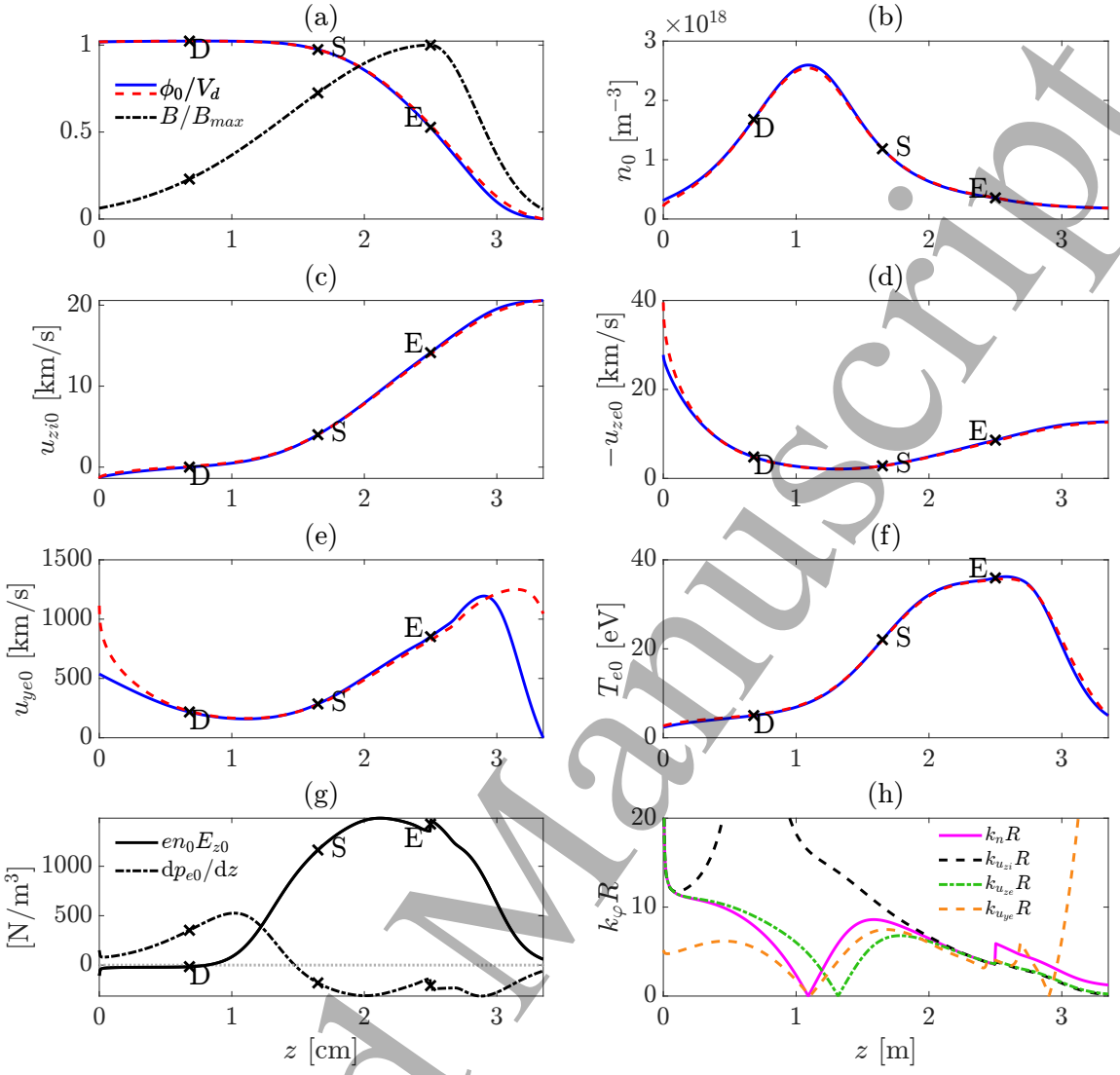

Figure 2: Stationary axial response of Model 0B for parameters in Table 1. Ion-stagnation (D), ion-sonic (S) and channel exit (E) are marked with crosses. Only $B(z)$ is an input, its maximum being at E. In (a)-(f), red dashed lines correspond to the inertialess-electron Model 0A. In (g): the two forces contributing to the azimuthal electron drift. In (h): relative gradient lengths of n, u_{zi}, u_{ze}, and u_{ye}.

velocity adapt, within a thin region, to the solution of Model 0A. Also, close to the anode, the near singularity of $\mathrm{d}u_{ye0}/\mathrm{d}z$ makes u_{ye0} significantly lower when inertia is considered; this reduction near the anode affects u_{ze0} too. For the rest of regions and plasma variables, Models 0A and 0B yield practically the same solution.

Neglecting the small collisional contribution to the axial momentum equation (17), this states that azimuthal electron velocity is approximately the sum of the $E \times B$ and diamagnetic drifts,

$$u_{ye0} = -\frac{1}{B}\left[\frac{\mathrm{d}\phi}{\mathrm{d}z} + \frac{1}{en_0}\frac{\mathrm{d}p_{e0}}{\mathrm{d}z}\right] > 0.$$

Figure 2(g) shows that each of these contributions dominates in separated regions of the

discharge and both yield an azimuthal current along $+y$ (notice that both drifts are negative only in regions where they are not dominant). The dominance of pressure gradients over the electric field in the inner part of the chamber, and the ion sonic transition there are two clear features highlighting the importance of electron pressure effects in an stability analysis of the global discharge.

A second aspect highlighting the importance of a global analysis is the high inhomogeneity of the equilibrium solution. Figure 2 (h) depicts the inverse of the local gradient length of main plasma magnitudes,

$$k_\varphi(z) = \left| \frac{1}{\varphi_0} \frac{\mathrm{d}\varphi_0}{\mathrm{d}z} \right| \tag{29}$$

for a generic plasma variable at equilibrium, φ_0. Leaving apart the singular behaviors near the anode sheath edge and the ion stagnation point ($u_{zi0} = 0$), the plasma profiles have $k_\varphi R = O(10)$. A local stability analysis is fully justifiable only for perturbation modes with axial wavenumbers k_z satisfying the Boussinesq approximation $k_z R \gg k_\varphi R = O(10)$. Otherwise only the global analysis of stability is fully consistent.

In order to evaluate spatial and time scales in the perturbation modes, typical values of the equilibrium solution are: $n_{e0} \sim 10^{18}$ m^{-3}, $T_{e0} \sim 20$ eV, $B \sim 150$ G, ion sound velocity $c_{s0} \sim 3.8$ km s^{-1}, electron thermal velocity $\bar{c}_{e0} \sim 1900$ km s^{-1}, cyclotron frequency $f_{ce} = \omega_{ce}/2\pi \sim 400$ MHz, lower-hybrid frequency $f_{lh} \sim 0.86$ MHz, axial-transit frequency $f_z \sim u_{zi0}/2\pi L_\mathrm{N} \sim 90$ kHz, azimuthal transit frequency $f_\theta \sim u_{ye0}/2\pi R \sim 3.5$ MHz, Debye length $\lambda_\mathrm{D} \sim 33$ μm, and electron gyroradius $\ell_e \sim 720$ μm. This yields $R/\ell_e \sim 60$ and $\ell_e/\lambda_\mathrm{D} \sim 22$.

2.2 Linear perturbation model

As aforementioned, the evolution of small perturbations to an equilibrium plasma is governed by the first-order expansion of equations (2)-(8). Nonetheless, perturbations of collision frequencies have been ignored (which is not fully consistent in all cases), as well as, the perturbations of neutral variables (which is correct for the high-frequency range of interest here). Then, the first order equations for continuity and momentum of ions and electrons are

$$u_{zi0}\frac{\mathrm{d}n_1}{\mathrm{d}z} + n_0\frac{\mathrm{d}u_{zi1}}{\mathrm{d}z} = \left(\mathrm{i}\omega - \frac{\mathrm{d}u_{zi0}}{\mathrm{d}z} + \nu_p - \nu_w\right) n_1 - \frac{\mathrm{d}n_0}{\mathrm{d}z}u_{zi1} \equiv F_1, \tag{30}$$

$$u_{ze0}\frac{\mathrm{d}n_1}{\mathrm{d}z} + n_0\frac{\mathrm{d}u_{ze1}}{\mathrm{d}z} = \left(\mathrm{i}\omega - \mathrm{i}k_y u_{ye0} - \frac{\mathrm{d}u_{ze0}}{\mathrm{d}z} + \nu_p - \nu_w\right) n_1 - \frac{\mathrm{d}n_0}{\mathrm{d}z}u_{ze1} - \mathrm{i}k_y n_0 u_{ye1} \equiv F_2, \tag{31}$$

$$u_{zi0}\frac{\mathrm{d}u_{zi1}}{\mathrm{d}z} + \frac{e}{m_i}\frac{\mathrm{d}\phi_1}{\mathrm{d}z} = \left(\mathrm{i}\omega - \frac{\mathrm{d}u_{zi0}}{\mathrm{d}z} - \nu_i\right) u_{zi1} \equiv F_3, \tag{32}$$

$$u_{ze0}\frac{\mathrm{d}u_{ze1}}{\mathrm{d}z} + \frac{T_{e0}}{m_e n_0}\frac{\mathrm{d}n_1}{\mathrm{d}z} - \frac{e}{m_e}\frac{\mathrm{d}\phi_1}{\mathrm{d}z} + \frac{1}{m_e}\frac{\mathrm{d}T_{e1}}{\mathrm{d}z} = \left(\mathrm{i}\omega - \mathrm{i}k_y u_{ye0} - \frac{\mathrm{d}u_{ze0}}{\mathrm{d}z} - \nu_e\right) u_{ze1} + \frac{eB}{m_e}u_{ye1} + \frac{T_{e0}}{m_e n_0^2}\frac{\mathrm{d}n_0}{\mathrm{d}z}n_1 - \frac{1}{m_e n_0}\frac{\mathrm{d}n_0}{\mathrm{d}z}T_{e1} \equiv F_4, \tag{33}$$

$$u_{ze0}\frac{\mathrm{d}u_{ye1}}{\mathrm{d}z} = (\mathrm{i}\omega - \mathrm{i}k_y u_{ye0} - \nu_e)\,u_{ye1} - \left(\frac{\mathrm{d}u_{ye0}}{\mathrm{d}z} + \frac{eB}{m_e}\right)u_{ze1} - \mathrm{i}k_y\frac{T_{e0}}{m_e n_0}n_1 + \mathrm{i}k_y\frac{e}{m_e}\phi_1 - \mathrm{i}k_y\frac{1}{m_e}T_{e1}, \tag{34}$$

and the energy equations for electrons are

$$\frac{\mathrm{d}q_{ze1}}{\mathrm{d}z} + \frac{3}{2}u_{ze0}n_0\frac{\mathrm{d}T_{e1}}{\mathrm{d}z} + \frac{3}{2}u_{ze0}T_{e0}\frac{\mathrm{d}n_1}{\mathrm{d}z} + \frac{5}{2}n_0T_{e0}\frac{\mathrm{d}u_{ze1}}{\mathrm{d}z} = \left(\mathrm{i}\omega\frac{3}{2}T_{e0} - \mathrm{i}k_y\frac{3}{2}u_{ye0}T_{e0} - \frac{3}{2}u_{ze0}\frac{\mathrm{d}T_{e0}}{\mathrm{d}z} - \frac{5}{2}T_{e0}\frac{\mathrm{d}u_{ze0}}{\mathrm{d}z} - \nu_p E_{\mathrm{inel}} - \nu_{we}T_{e0} + m_e\nu_e u_{ye0}^2\right)n_1 + \left(-\frac{3}{2}\frac{\mathrm{d}n_0T_{e0}}{\mathrm{d}z} + 2m_e\nu_e n_0 u_{ze0}\right)u_{ze1} + \left(-\mathrm{i}k_y\frac{5}{2}n_0T_{e0} + 2m_e\nu_e n_0 u_{ye0}\right)u_{ye1} + \left(\mathrm{i}\frac{3}{2}\omega - ik_y\frac{3}{2}u_{ye0} - \frac{3}{2}\frac{u_{ze0}}{n_0}\frac{\mathrm{d}n_0}{\mathrm{d}z} - \frac{5}{2}\frac{\mathrm{d}u_{ze0}}{\mathrm{d}z} - \nu_{we} - \frac{5}{2}\frac{T_{e0}}{m_e\nu_e}k_y^2\right)n_0T_{e1} + \mathrm{i}k_y\frac{\omega_{ce}}{\nu_e}q_{ze1}, \tag{35}$$

$$\frac{5}{2}n_0T_{e0}\frac{\mathrm{d}T_{e1}}{\mathrm{d}z} = -\frac{5}{2}T_{e0}\frac{\mathrm{d}T_{e0}}{\mathrm{d}z}n_1 - \frac{5}{2}n_0\left(\frac{\mathrm{d}T_{e0}}{\mathrm{d}z} + ik_y\frac{\omega_{ce}}{\nu_e}T_{e0}\right)T_{e1} - m_e\frac{\nu_e^2+\omega_{ce}^2}{\nu_e}q_{ze1} \equiv F_5, \tag{36}$$

Under the limits of cold electrons (implying hypersonic ions) and

$$\mathrm{d}u_{zi0}/\mathrm{d}z,\ k_z u_{zi0},\ k_z u_{ze0} \ll \omega,\ k_y u_{ye0},\ \nu_e \ll \omega_{ce}$$

(with k_z an effective axial wavenumber) the mathematical complexity of the problem gets significantly reduced and the perturbation problem resembles the one by Escobar and Ahedo [14]. Furthermore, if electron collisions are assumed to be even smaller (i.e., $\nu_e \ll \omega, k_y u_{ye0} \ll \omega_{ce}$) the perturbation problem becomes collisionless and similar to that of Sorokina et al. [19].

The boundary conditions for the perturbation model are perturbations of those for the equilibrium problem, and are homogeneous for the stability analysis. They are the following.

1. The ion velocity satisfies the Bohm condition at B,

$$u_{zi1\mathrm{B}} = -\frac{c_{s0\mathrm{B}}}{2T_{e0\mathrm{B}}}T_{e1\mathrm{B}} = -\frac{1}{2m_i c_{s0\mathrm{B}}}T_{e1\mathrm{B}}. \tag{37}$$

   As it will be shown, the first-order problem is singular at the anode-sheath edge. This condition ensures the validity of the small-perturbation assumption close to the anode singularity [32]. The numerical solution of the perturbation problem verifies that this is required for moderate growths of perturbations around B and for good convergence behaviour with a suitable number of grid points.

2. The potential perturbation is zero at the anode, $\phi_{1\mathrm{A}} = 0$. Then, assuming an instantaneous response of the anode sheath to perturbation, the linearized sheath potential-fall condition yields

$$\phi_{1\mathrm{B}} = \phi_{1\mathrm{A}} + \left(\frac{e\phi_{0\mathrm{AB}}}{T_{e0\mathrm{B}}} + \frac{1}{2}\right)\frac{T_{e1\mathrm{B}}}{e} - \frac{T_{e0\mathrm{B}}}{eu_{ze0\mathrm{B}}}u_{ze1\mathrm{B}}. \tag{38}$$

3. The heat flux at the sheath edge satisfies

$$q_{ze1\mathrm{B}} = \left(e\phi_{0\mathrm{AB}} - \frac{1}{2}T_{e0\mathrm{B}}\right) u_{ze0\mathrm{B}} n_{1\mathrm{B}} + \left(e\phi_{0\mathrm{AB}} - \frac{3}{2}T_{e0\mathrm{B}}\right) n_{0\mathrm{B}} u_{ze1\mathrm{B}} + \frac{e\phi_{0\mathrm{AB}}}{T_{e0\mathrm{B}}} n_{0\mathrm{B}} u_{ze0\mathrm{B}} T_{e1\mathrm{B}}. \quad (39)$$

4. A regularizing boundary condition at point S is required to ensure smooth behaviour close to the sonic point, similarly to the equilibrium problem. The system of first order fluid equations written in the form of equations (30)-(36) hides the role played by sonic points in the model. From equations (30)-(33) and (36), the derivative of u_{zi1} satisfies

$$n_0 \left(T_{e0} - m_i u_{zi0}^2\right) \frac{\mathrm{d}u_{zi1}}{\mathrm{d}z} = G_1,$$
$$G_1 = T_{e0}F_1 + m_e u_{ze0} u_{zi0} F_2 - n_0 u_{zi0} \left(m_i F_3 + m_e F_4 - \frac{2}{5}\frac{F_5}{n_0 T_{e0}}\right),$$

where $u_{ze0} \ll \bar{c}_{e0}$ was used, and functions F_1 to F_5 are defined in equations (30)-(33) and (36), respectively. Thus

$$G_{1\mathrm{S}} = 0 \quad (40)$$

is required to avoid a singularity at the zeroth-order interior sonic point in the perturbation problem (the anode-sheath edge is, however, singular). The interior sonic point of the perturbed plasma is shifted with respect to the zeroth-order position [32] but this displacement is not needed to solve the perturbation problem and can be computed in post-processing.

5. The perturbation of the discharge current is zero at the cathode,

$$I_{d1\mathrm{N}} \equiv A_{e\mathrm{N}} e \left[(u_{zi0\mathrm{N}} - u_{ze0\mathrm{N}}) n_{1\mathrm{N}} + n_{0\mathrm{N}} u_{zi1\mathrm{N}} - n_{0\mathrm{N}} u_{ze1\mathrm{N}}\right] = 0. \quad (41)$$

The alternative case of zero perturbation of the cathode potential, $\phi_{1\mathrm{N}} = 0$, will be treated later too.

6. The azimuthal electron velocity perturbation is zero at the cathode, $u_{ye1\mathrm{N}} = 0$.

7. The temperature of electrons injected at N is known, yielding $T_{e1\mathrm{N}} = 0$.

For a given equilibrium solution, the parameters of the linear perturbation problem (defined in the complex plane) are the real wavenumber k_y and the complex frequency $\omega \equiv \omega_r + \mathrm{i}\gamma$. For each k_y, the problem admits eigenvalues ω and eigenmodes (i.e. non-trivial solutions) in the form of the perturbation magnitudes $\varphi_1(z, k_y, \omega)$ in equation (13). Eigenmodes with $\gamma > 0$ are unstable. Modes with phase velocity $\omega_r/k_y > 0$ propagate in the $+u_{ye0}$ (i.e $+y$) direction. It is enough to analyze the parametric region $k_y > 0$ since, as demonstrated in Appendix B, the region $k_y < 0$ yields the same perturbation m The numerical method to solve this eigenvalue (or Sturm-Liouville) problem is explained in the Appendix C.

3 Near-plume and near-anode instabilitiess

Stability results will be hereafter analyzed for several simulation settings. This and next section discuss a, say, *nominal model* (or Model I) consisting of (i) the stationary,

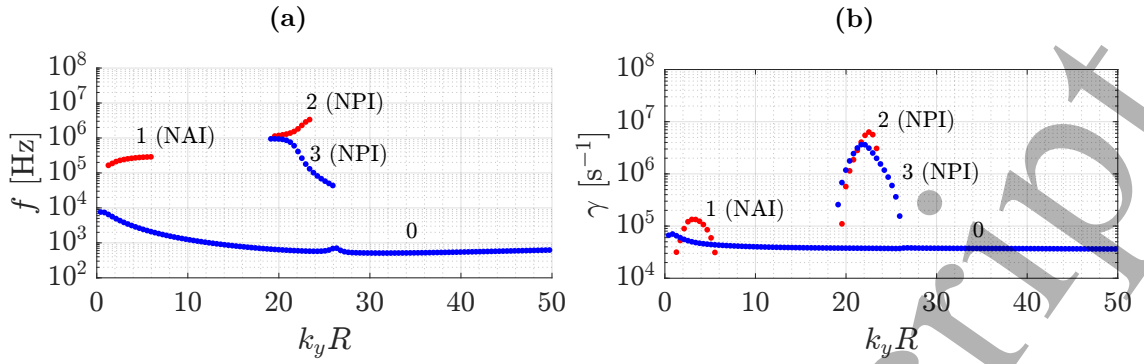

Figure 3: Nominal model. Main eigenvalues of global dispersion relation. Each unstable branch is tagged with a number and an instability type. Red and blue colours denote propagation along $+y$ and $-y$, respectively.

inertialess-electron Model 0A, and (ii) the perturbation model with zero electron temperature perturbations (i.e. $T_{e1} = 0$), thus consisting of Eqs. (30)-(34), and (iii) the perturbed boundary conditions defined before. Parameters of table 1 will be used, except in sections 4.3 and 4.4, devoted to parametric investigation where the effects of varying the magnetic field slope, the discharge voltage, the mass flow and the channel length, are analyzed. Three off-nominal models (II, II, and IV) are defined and discussed in Section 5.

In Sturm-Liouville problems, such as the present one, the number of eigenvalues of the global dispersion relation can be, in principle, infinite. The interest is, of course, in the most unstable modes. The instability analysis here will be centered in unstable modes with: (real) frequencies $f = |\omega_r|/2\pi \sim 0.5-50$ MHz, well below the electron gyrofrequency ($\omega_{ce}/2\pi \sim 400$ MHz); and azimuthal mode numbers $k_y R < 50$ (i.e azimuthal wavelengths down to $\lambda_y \equiv 2\pi/k_y \sim 5$ mm), also within the applicability range of the present fluid formulation.

The unstable solutions of the dispersion relation for the nominal model are plotted in figure 3. There are up to 3 families of high-frequency unstable modes plus a low-frequency ($f \sim 7.5$ kHz) unstable family. This last one [branch 0 in figure 3] is characterized by intense density oscillations in the ionization region, which correspond to the breathing and rotating-spoke modes of Ref. [13] but incompletely characterized in the present mid-to-high frequency model (which neglects neutral density perturbations). Hereafter that low-frequency mode will be omitted from figures and discussions.

Then, in the range $f > 100$ kHz of interest, there are three branches of unstable modes. Based on the region where these modes develop preferentially, they are named Near-Anode Instability (NAI) [branch 1 in figure 3] and Near-Plume Instability (NPI) [branches 2 and 3]. Figure 3 states that the global perturbation response of the nominal model is dominated by the NPI mode in branch 2 with $k_y R = 23$ (i.e. $\lambda_y = 1.16$ cm) and $f = 2.87$ MHz. In addtion, the NAI mode of branch 1 with $k_y R = 3$ (i.e. $\lambda_y = 8.90$ cm) and $f = 241$ kHz is considered a subdominant mode, since it develops in a different region of the discharge and thus can still be present in the long-time response. Branch 3 is just a second NPI mode, likely overshadowed by branch 2 in the long-time response.

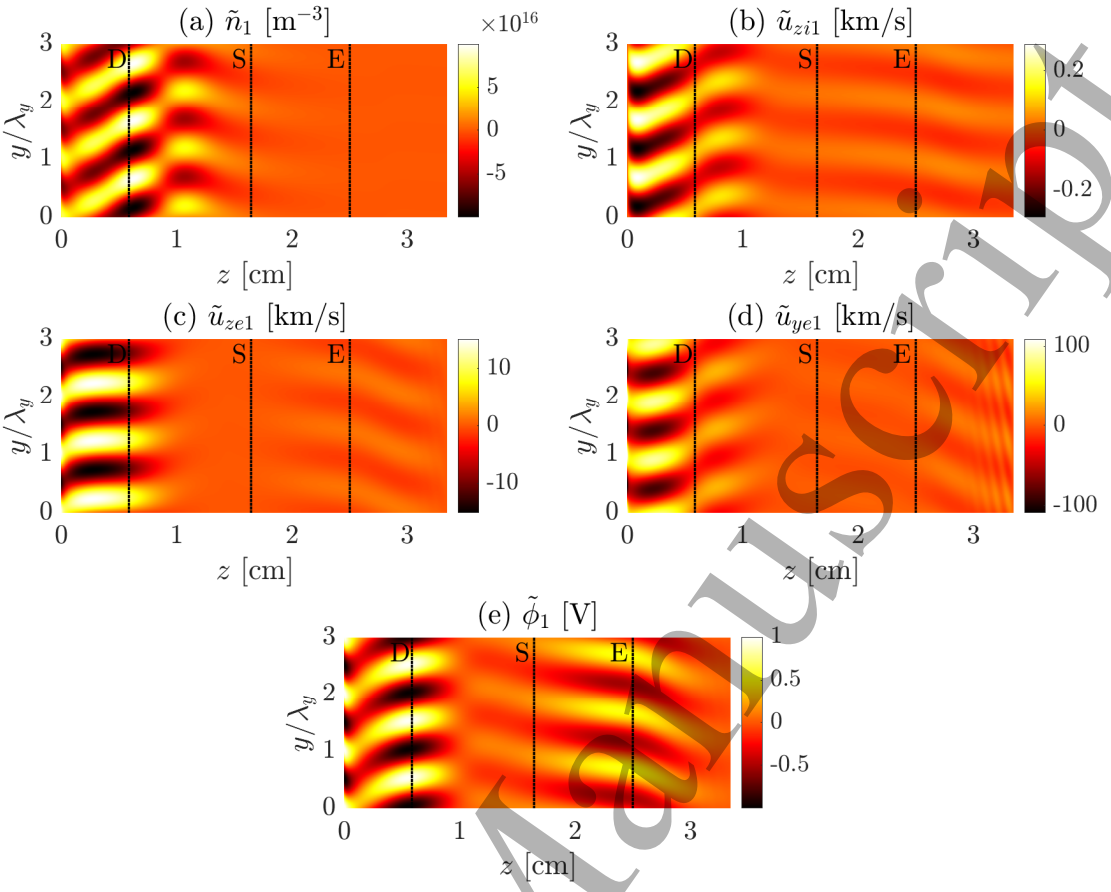

Figure 4: Nominal model. Instantaneous spatial response for the subdominant NAI mode, with $k_yR = 3$ and $f = 241$ kHz. In this and similar figures, only three azimuthal wavelengths are plotted and perturbations amplitudes correspond to $\tilde{\phi}_{1,\max} = 1$ volt.

3.1 The subdominant Near-Anode Instability

The NAI in figure 3 presents low azimuthal mode numbers, $k_yR = 1.3$-6.0 ($\lambda_y \sim 4.4$-21 cm), and mid-frequencies $f = 160$-290 kHz. Instantaneous 2D spatial profiles of the main NAI mode ($k_yR = 3$) are shown in figure 4. The plots represent perturbation solutions, i.e. the eigenmodes defined in equation (13). They scale linearly with, say,

$$\tilde{\phi}_{1,\max} = \max\{\tilde{\phi}_1(y,z,t)\}\ \forall y,z. \tag{42}$$

which has been set to equal to 1 volt in figure 4.

It is clearly observed that the NAI develops mainly in the near-anode region (from B to D in figure 2), but some remnants are observed in the rest of the discharge, in particular for $\tilde{\phi}_1$ around the thruster exit E. Azimuthally, the NAI propagates with an azimuthal phase velocity $\omega_r/k_y = 21.5$ km/s for $k_yR = 3$ in the $+u_{ye0}$ direction; remind that this velocity is a diamagnetic drift near the anode. The axial propagation of the NAI is not identical for all plasma variables as the change of inclination of the wavefronts in figure 4 illustrates. A Fast Fourier transform (FFT) analysis discussed later will identify the main axial wavenumbers k_z of the perturbed variables. Near the anode, $\tilde{n}_1$, $\tilde{u}_{zi1}$, and $\tilde{\phi}_1$ propagate axially outwards (i.e., the dominant term in the FFT has $k_z < 0$), while electron

velocities do not propagate. Around the chamber exit, the propagation of $\tilde{\phi}_1$ has changed and is directed towards the plume (i.e. $k_z > 0$).

The high-frequency global analysis by Sorokina et al. [19] discusses the existence of a near-anode modes with $k_y R$ from 1 to 5, frequencies of 260-670 kHz and propagation in the $+u_{ye0}$ direction. There are however differences with the present case, that could be related to model limitations (some of them also common to the global models of [14] and [20]), such as the lack of pressure forces on both the equilibrium and perturbation problems and the assumption of marginal electron inertia effects. Also, the local analysis by Marusov et al. [33] predicts near-anode instabilities within similar frequency range and suggests that pressure force has a non-negligible impact on the resultant wavelengths, frequencies and growth rates of the unstable modes.

Rotating-spoke instabilities are also near-anode oscillations propagating in the $+u_{ye0}$ direction with similar λ_y but generally at frequencies below 100 kHz [2, 34]. An exception are rotating spokes with $f \sim$ 79-210 kHz observed in a cylindrical HET [35]. This discrepancy with respect to experimentally observed frequencies of near-anode modes was already noted in reference [19]. The formation of wave packets with a reduced envelope frequency, when unstable modes with similar ω_r and γ co-exist, was identified as a possible explanation.

3.2 The dominant Near-Plume Instability

For the nominal model, figure 3 shows that the main NPI branch [number 2 in figure 3] develops at higher mode numbers and frequencies than the NAI. It has $k_y R \sim$ 19-23 (i.e., $\lambda_y \sim$ 1.40-1.16 cm), and $f \sim$ 1.1-3.3 MHz. The azimuthal propagation is along $+u_{ye0}$, which is now due to the $E \times B$ drift. Instantaneous 2D spatial profiles of the dominant NPI mode, with $k_y R \sim 23$ and $f = 2.87$ MHz (thus, $\omega/k_y \simeq 45.9$km/s) are shown in figure 5. The oscillations develop almost exclusively in the near plume, which coincides here with the region having $\mathrm{d}B/\mathrm{d}z < 0$. Concerning the direction of propagation of the waves, $\tilde{n}_1$ and $\tilde{u}_{zi1}$ propagate obliquely inwards (i.e. with positive k_z). The propagation of $\tilde{\phi}_1$, $\tilde{u}_{ze1}$ and $\tilde{u}_{ye1}$ is azimuthal. For $\tilde{u}_{ye1}$, there is an abrupt change of phase, close to 180°, at the mid-plume. This event takes place when $\mathrm{d}\tilde{\phi}_1/\mathrm{d}z$ changes sign, due to the inversion of the azimuthal $E \times B$ drift component in the perturbation problem. Additionally, $\tilde{u}_{ye1}$ presents small-amplitude short-wavelength axial waves.

The NPI modes of branch 3 in figure 3 propagate azimuthally along $-y$. Since they develop in the same discharge region of branch 2 with a smaller γ they will not be observed in the long-term perturbed plasma response, so they are dropped from the discussion here.

The NAI and NPI modes present interesting differences on the relative perturbations of the different plasma magnitudes. First, $\tilde{n}_1/\tilde{\phi}_1$ and $\tilde{u}_{zi1}/\tilde{\phi}_1$ decrease by two orders of magnitudes from the NAI to the NPI, suggests that the NPI is mainly an 'electron mode'. Second, $\tilde{n}_1/n_0 \ll e\tilde{\phi}_1/T_{e0}$ for the NPI mode, which has consequences on fulfilling quasineutrality (see Sec. 4.1). Third, while the NAI has $\tilde{u}_{ze1} \ll \tilde{u}_{ye1}$, the NPI has $\tilde{u}_{ze1} \sim \tilde{u}_{ye1}$, implying that $\tilde{u}_{ze1}/u_{ze0} \gg \tilde{u}_{ye1}/u_{ye0}$, so that the perturbed axial electron inertia is as relevant as the azimuthal one for the NPI mode (see Sec. 6.1).

The development of oscillations in the discharge region where $\mathrm{d}B/\mathrm{d}z < 0$ suggest a connection of the (global) NPI with (local) high-frequency drift-gradient instabilities [23, 28, 33], originally analyzed by Esipchuk and Tilinin [31]. The dispersion relation for these waves points at density and magnetic gradients as the main instability mechanisms. In the local

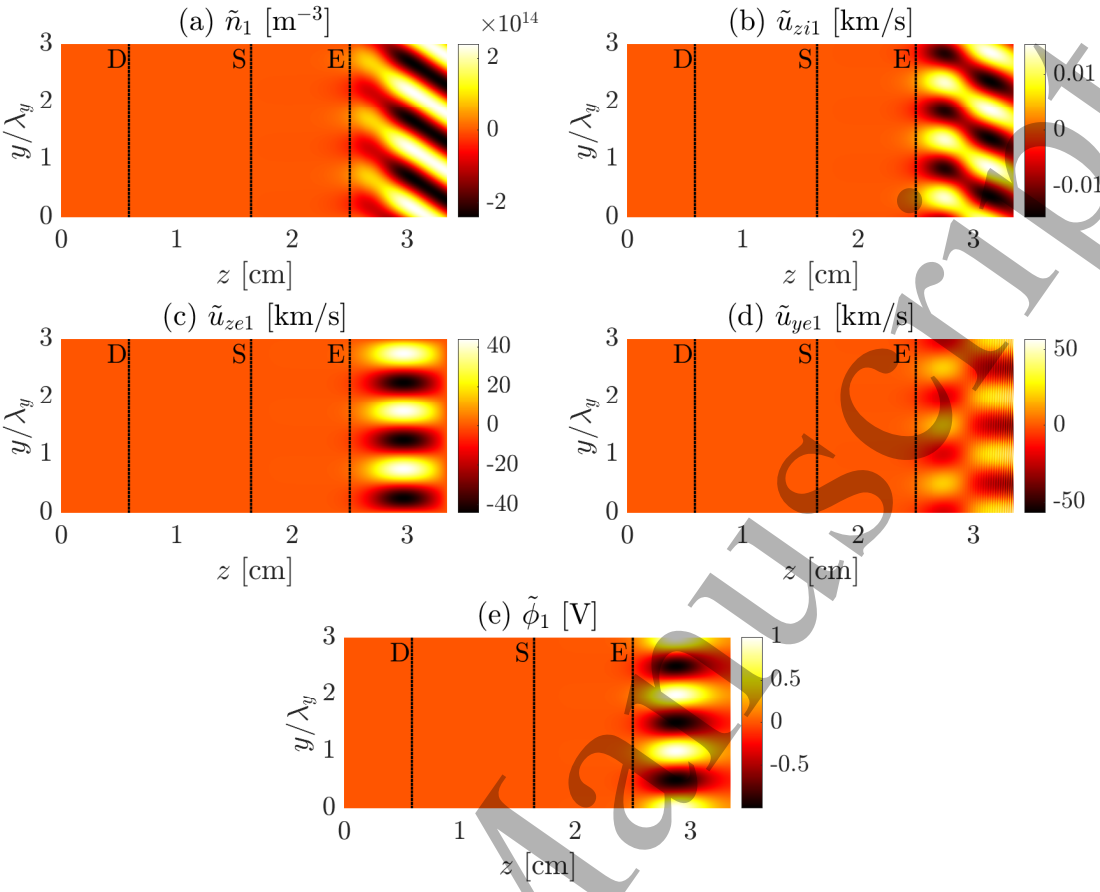

Figure 5: Nominal model. Instantaneous spatial response for the dominant NPI mode: $k_y R = 23$ (i.e. $\lambda_y = 1.16$ cm) and $f = 2.87$ MHz.

stability analyses, the values of $\mathrm{d}B/\mathrm{d}z$ and $\mathrm{d}n_0/\mathrm{d}z$ leading to instabilities do not follow simple criteria and depend on the model assumptions and other local properties of the plasma. For example, the local analysis by Marusov et al. [33] shows near-plume drift-gradient modes, within the wide frequency range 0.01-12.16 MHz, that are only unstable when accounting for finite electron temperature. The effect of the magnetic field shape on the NPI modes is further investigated later.

Finally, counter-propagating azimuthal oscillations have been observed in some empirical results in the literature [36], which resemble the main and secondary NPI modes here. These observations have been made in the frequency range 0.9-6 MHz, but in the context of the electron-cyclotron drift instability. The azimuthal scales are smaller, generally satisfying $k_y \ell_e \gtrsim O(1)$, outside the range of analysis of the fluid models here.

4 Further investigation of the NAI and NPI instabilities

This section analyzes more in detail the characteristics of the NAI and NPI modes for the nominal model.

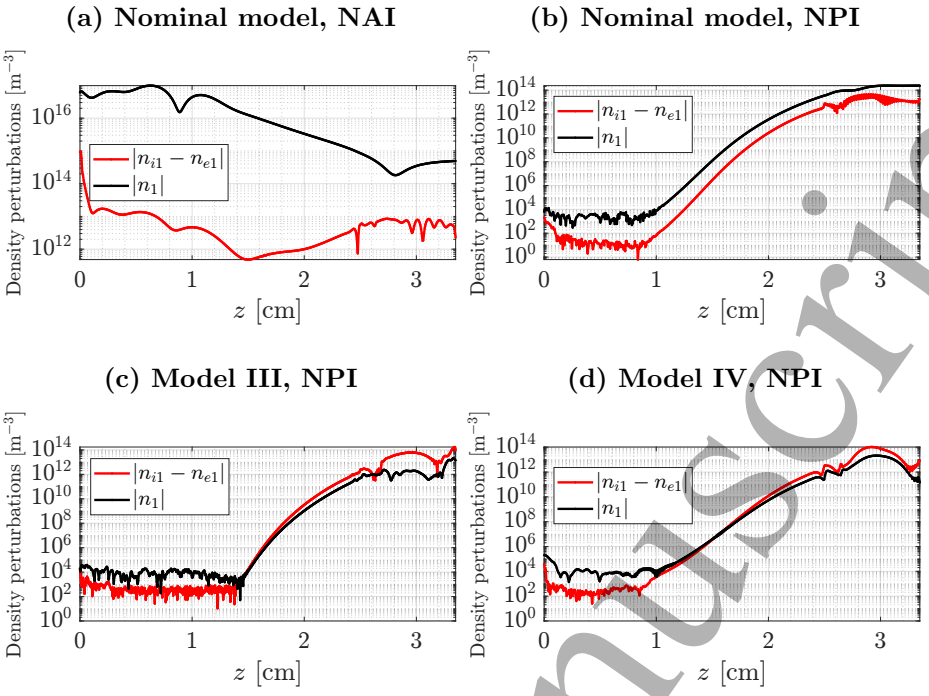

Figure 6: Assessment of quasineutrality in main instability modes. (a) Subdominant NAI in nominal model. (b) Dominant NPI in nominal model. (c) Dominant NPI in Model III, having $k_y R = 37.4$ and $f = 27.2$ MHz. (d) Dominant NPI in Model IV, having $k_y R = 25.1$, $f = 14.2$ MHz. The noise in the electric charge is due to the numerical second derivative of ϕ_1 used for its computation.

4.1 Plasma quasineutrality

The perturbation model has assumed the zero-Debye length limit, so perturbations are quasineutral except in the perturbed anode sheath. Once the solution is known, the level of compliance with quasineutrality can be assessed. The perturbed Poisson equation allows to estimate the charge separation as

$$e\left(n_{i1} - n_{e1}\right) = \varepsilon_0 \left(k_y^2 \phi_1 - \frac{\mathrm{d}^2 \phi_1}{\mathrm{d}z^2}\right), \tag{43}$$

and to compare it with the quasineutral estimated charge density, en_1. A value of λ_D, based on n_0 and T_{e0}, very small compared to any other characteristic length of the problem is enough to ensure the validity of the quasineutral assumption in the equilibrium solution. For the $k_y R$ range considered in this work, $k_y \lambda_\mathrm{D}$ is always very small. However, in the first-order problem, and assuming $k_z \leq O(k_y)$, quasineutrality requires

$$k_y \sqrt{\varepsilon_0 \phi_1 / e n_1} \ll 1, \tag{44}$$

which is a more severe condition than $k_y \lambda_\mathrm{D} \ll 1$ when $n_1/n_0 \ll e\phi_1/T_{e0}$, a situation happening for the dominant NPI.

For the NAI and the NPI modes of the nominal model, figure 6 (a) and (b) plot both $(n_{i1} - n_{e1})$ and n_1, showing that $|n_{i1} - n_{e1}| \ll |n_1|$, thus validating the modes are quasineutral.

However, figures 6(c)-(d) for off-nominal models discussed in section 5, will show that the dominant NPI modes present non-neutral effects, which should be included in the global perturbation model. That inclusion is far from immediate since the perturbation model is built upon a stationary solution which is quasineutral, except for the anode sheath.

4.2 Axial wavenumbers

A standard *local* stability analysis solves the complex eigenfrequency for given azimuthal and axial wavenumbers, that is $\omega(k_y, k_z)$. The present global stability analysis provides the complex eigenfrequency for each azimuthal wavenumber $\omega(k_y)$ and the complex eigenmodes as functions of z. These eigenmodes do not correspond generally to normal modes with a single k_z. Indeed, the analysis of the NAI and the NPI in figures 4 and 5, respectively, showed that the axial propagation is dependent on both the variable and the region within the discharge.

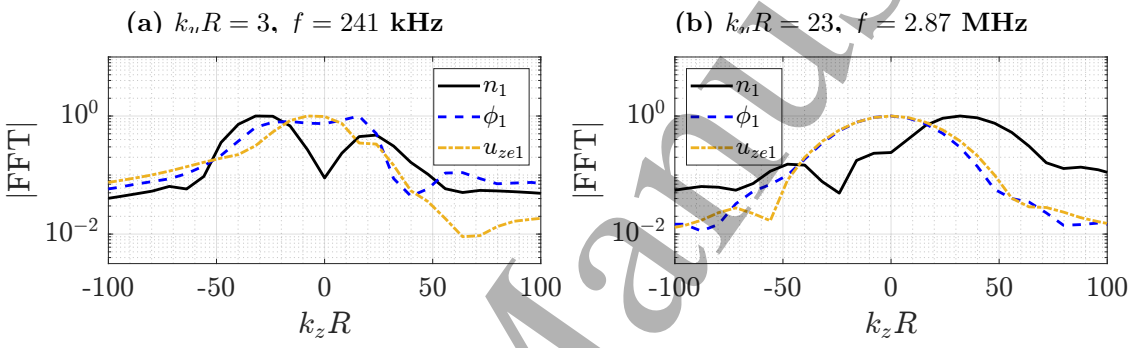

Figure 7: Nominal model. Axial wavenumbers of n_1, ϕ_1 and u_{ze1} from the (normalized) axial FFT of the perturbed solution, for (a) the subdominant NAI mode and (b) the dominant NPI mode.

The dominant axial wavenumbers of the instability modes can be obtained from the axial FFT. The k_zR-spectrum goes from a minimum of $2\pi R/L_{\mathrm{N}} \simeq 8$ to a maximum of $\pi R/\Delta z \approx 4000$, where $\Delta z \approx L_{\mathrm{N}}/1000$ is the cell size used here to solve the Sturm-Liouville problem. The axial FFTs of the modes of figures 4 and 5 are plotted in figure 7. The FFTs are done on complex amplitudes and yield, in general, nonsymmetrical spectra on k_z for each k_y. The sign of the dominant k_z determines the principal direction of axial propagation. The FFTs in figure 7 for each global mode show that the dominant k_z is different for several perturbation variables. The trends already identified in figures 4 and 5 are confirmed here: for the NAI, the negative oblique propagation of $\tilde{n}_1$, the positive and negative oblique propagations of $\tilde{\phi}_1$, and the purely-azimuthal propagation of $\tilde{u}_{ze1}$; for the NPI, the positive oblique propagation of $\tilde{n}_1$, a secondary high-k_z mode on electron velocities (out of the k_zR limits of the figure), etcetera. The comparison of figures 2(h) and 7, yields that the Boussinesq approximation, $k_z \gg k_\varphi$, that could justify a local axial analysis, is not satisfied.

4.3 Influence of the magnetic field slope

The previous analysis has shown that the NPI develops only outside point E, which, for the chosen configuration, is both the thruster chamber exit and the location of the maximum magnetic field. In this subsection the location of B_m is shifted away from the

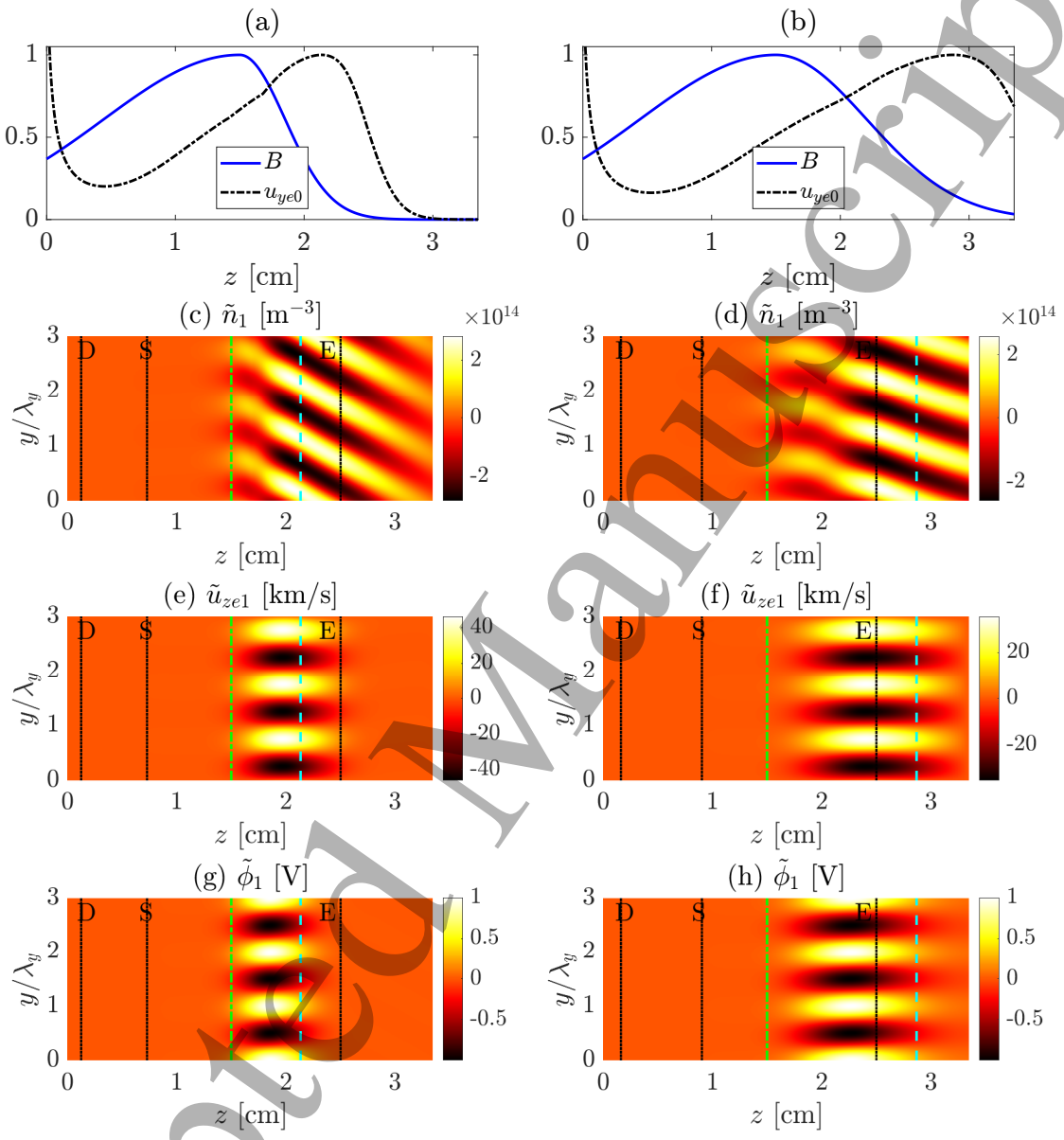

Figure 8: Nominal model. Variation of the magnetic field profiles. In left plots, the magnetic field has $(z_m, L_{m,\text{out}}) =$ (1.5 cm, 0.5 cm), and the dominant NPI eigenmode has $(k_y R, f) =$ (25.1, 2.36 MHz). In right plots, one has $(z_m, L_{m,\text{out}}) =$ (1.5 cm, 1 cm) and $(k_y R, f) =$ (15.3, 1.46 MHz). First row: Axial profiles of B and the stationary azimuthal electron velocity. Rows 2 to 4: instantaneous profiles of the dominant mode. Green dash-dotted and cyan dashed vertical lines indicate the locations of the maxima of B and u_{ye0}, respectively.

chamber exit (still point E) in order to elucidate whether the change of the plasma jet area and collisionality or, more likely, the slope of $B(z)$ are driving the NPI. All the equilibrium plasma variables are recomputed in every case according to the equilibrium equations in section 2.1. Figure 8 shows the dominant NPI mode for two magnetic profiles with $z_m = 1.5$ cm, i.e. 1 cm inwards of E. The left case keeps constant the axial decay length $L_{m,\text{out}}$, and the right one smooths that decay. The corresponding dominant NPI modes have $(k_y R, f)$ equal to (25.1, 2.36 MHz) and (15.3, 1.46 MHz), respectively. In the first row, together with $B(z)$, $u_{ye0}(z)$ is depicted, showing a maximum to the right of z_m. The other three rows plot the perturbation solution for the dominnat NPI mode showing that while $\tilde{n}_1$ and (unplotted) $\tilde{u}_{zi1}$ oscillations spread all over the $\mathrm{d}B/\mathrm{d}z < 0$ region, the electron-related oscillations are bounded approximately between the maxima of $B(z)$ and and $u_{ye0}(z)$. The eigenvalue spectrum of the case with the slowest decay of $B(z)$ (unplotted), shows a significant shift of the NPI to smaller wavelengths $k_y R \sim$ 13-19. The behavior of the NPI under variations of $B(z)$ reinforces the idea that these modes are strongly related with $\mathrm{d}B/\mathrm{d}z$ being negative. Local fluid instabilities, in the same order of frequencies, driven by negative gradients of B (and n_0) were studied by Esipchuk and Tilinin [31] and have been recently revisited by several authors [23, 28].

4.4 Investigation of operation and geometrical parameters

In order to check the dependence of the NAI and NPI on the zeroth-order solution, the perturbation problem is solved for different equilibrium solutions, obtained by modifying discharge voltage, mass flow, or channel length. In order to have in each case an optimal magnetic strength (with the plasma well attached to the anode) the maximum amplitude of the magnetic field is tuned according to conditions of reference [12]. In each case, the rest of parameters are as in table 1.

Figure 9 (top row) plots the influence of the discharge voltage, through cases $V_d = 200$ V, 300 V and 700 V. The NAI is favored by a low V_d, when its range of $k_y R$ is wider and the growth rate is larger; its frequency increases slightly with V_d. The NAI is practically absent for $V_d = 700$ V. As suggested before, those features are typical of rotating spoke instabilities, as reported experimentally [37] and numerically [13]. With respect to the NPI modes, as V_d increases, there is a shift on $k_y R$ toward higher wavenumbers but both the amplitude of the $k_y R$-range and the maximum growth rate do not change practically. The frequency increases slightly with V_d, which agrees with empirical evidence on high-frequency oscillations in Hall thrusters [38].

Figure 9 (middle row) plots the influence of the mass flow rate, simulating three different flows. For the NAI, the $k_y R$ range is very sensitive to $\dot{m}$: at low values, the NAI disappears; at high values, the range becomes wide and can even overlap the one of the NPI. At low mass flows, the frequency of the oscillations decreases mildly. Similar trends were identified in reference [13] for rotating spokes due to the displacement of the ionization region. Nonetheless, NPI continues to be the dominant mode and presents a mild shift of $k_y R$ with mass flow changes.

Figure 9 (bottom row) plots the influence of the channel length, L_E, while keeping constant the distance from exit to cathode (i.e. $L_\text{N} - L_\text{E}$). The ratio $B(0)/B_m$ is also kept constant throughout the cases, by adjusting $L_{m,\text{in}}$, in order to prevent the long-channel case from having unrealistically low magnetic field close to the anode. The NAI gets less unstable as the channel is shorter and, indeed, that unstable branch disappears for $L_\text{E} = 1.4$ cm. This is coherent with findings on the rotating spoke: they were observed originally in

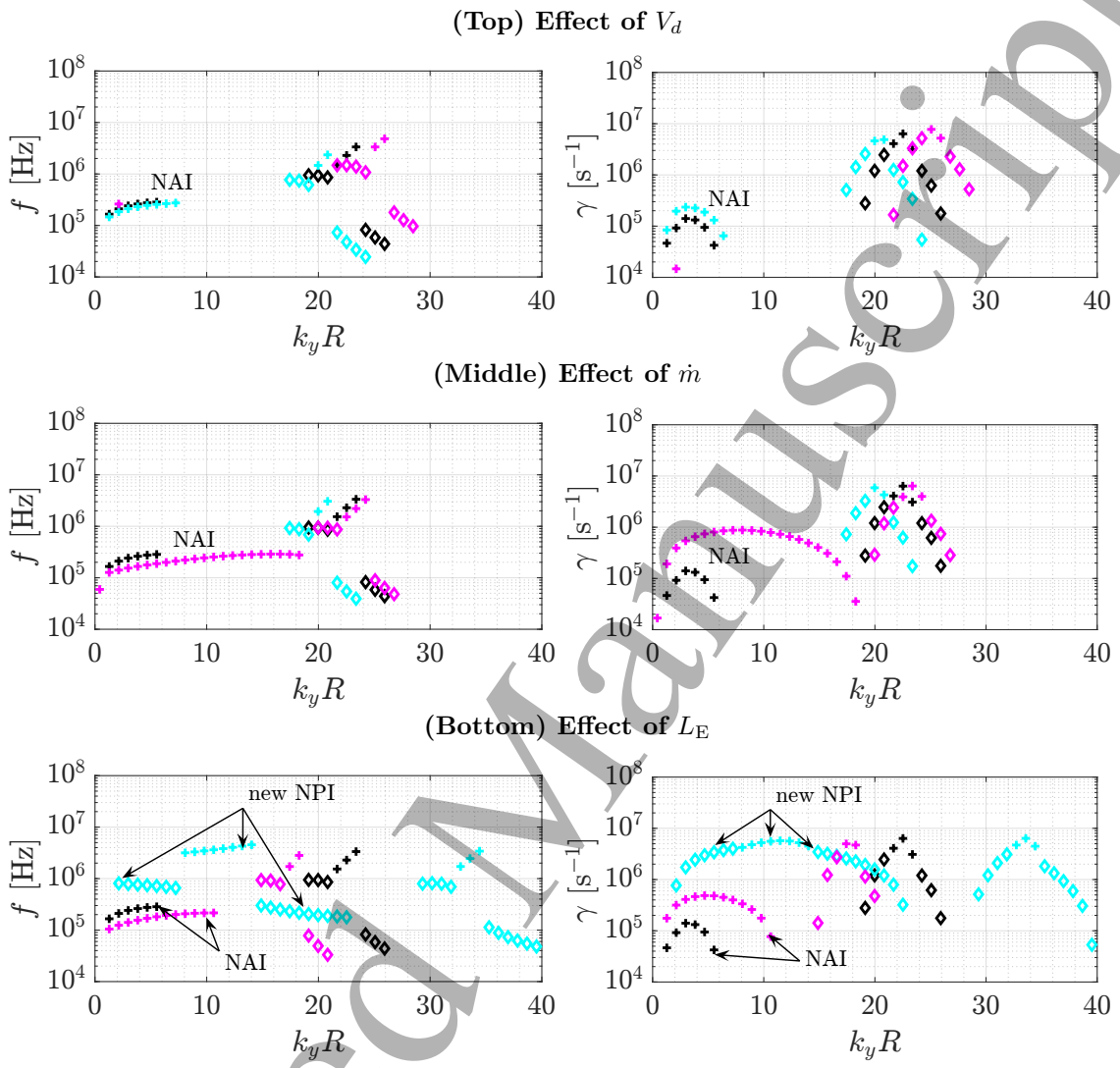

Figure 9: Nominal model. Effects on the dispersion relation of parametric variation. In each case, parameters of table 1 are used except those explicitly specified below. Contrary to other similar figures, for each case, only the most unstable mode at each k_yR is plotted. All eigenvalues correspond to NPI modes, except those specifically marked. Cross and diamond markers account for azimuthal propagation in the $+y$ and $-y$ directions, respectively. (Top) Effect of discharge voltage: $V_d = 200$ V, $B_m = 194$ G (cyan); $V_d = 300$ V, $B_m = 251$ G (black, nominal case); and $V_d = 700$ V, $B_m = 416$ G (magenta). (Middle) Effect of node mass flow: $\dot{m} = 3.1$ mg/s, $B_m = 224$ G (cyan); $\dot{m} = 4.75$ mg/s, $B_m = 251$ G (black, nominal case); and $\dot{m} = 6.3$ mg/s, $B_m = 265$ G (magenta). (Bottom) Effect of the channel length: $L_{\mathrm{E}} = 1.4$ cm, $B_m = 245$ G (cyan); $L_{\mathrm{E}} = 2.5$ cm, $B_m = 251$ G (black, nominal case); and $L_{\mathrm{E}} = 3.3$ cm, $B_m = 251$ G (magenta).

a long-channel ($\sim$ 10 cm) thruster [2] and PIC simulations suggest that they appear if the anode-cathode distance is large enough [3]. The frequency and growth rate of the dominant NPI do not change much with the chamber length but the mode number k_yR shifts towards higher values when reducing L_E as a consequence of modifying the decay of $B(z)$ inside the channel. This points out that the near-plume instability is not totally alien to gradients inside the chamber. An interesting novelty is the presence, for the shortest channel, of a new pair of NPI branches with lower wavenumbers ['new NPI' in figure 9(bottom row)]. Interestingly, their dominant mode has a growth rate very close to the one of the original pair of NPI branches, and will also be found again next.

5 Changes in the global fluid models

The following off-nominal models, named II, III and IV, are considered here. In section 5.1, Model II corresponds to the nominal one except for a change of a boundary condition in the perturbation model. In section 5.2, Model III corresponds to the nominal one except for the stationary Model 0B being used instead of the (electron inertialess) Model 0A. And in section 5.3, Model IV corresponds to the nominal one except that T_{e1} perturbations are admitted in the perturbation model.

5.1 Model II: Change of the circuit boundary condition

Depending on the anode-to-cathode electric circuit coupled to the plasma, the discharge current or the discharge voltage are controlled. When solving the stationary problem, this is not an issue, since results will be the same as long as the operational point in the current-voltage curve of the thruster model is the same. However, fixing the current or voltage does affect time-dependent perturbations and the global stability dispersion relations can present differences. The nominal model here has considered a current-controlled response with $I_{d1\mathrm{N}} = 0$, Eq. (41). Model II here changes from the boundary condition $I_{d1\mathrm{N}} = 0$ to $\phi_{1\mathrm{N}} = 0$ (which together with $\phi_{1\mathrm{A}} = 0$, guarantees $V_{d1} = \phi_{1\mathrm{A}} - \phi_{1\mathrm{B}} = 0$).

Figure 10 depicts main eigenvalues of the global dispersion relation for this voltage-controlled case. The known branches 1 to 3 of the nominal model are just shifted moderately, with no qualitative changes in the NAI and NPI modes. The most unstable mode in branch 2 has now $k_yR = 25.5$, $f = 2.04$ MHz, $\gamma = 5.73 \cdot 10^6$ s^{-1}. Beyond that, two additional branches, 4 and 5, of NPI type, appear, qualitatively identical to the ones found in figure 9(bottom) for the short-channel. The main NPI mode in branch 4, has $k_yR = 11.0$, $f = 3.0$ MHz, and $\gamma = 6.16 \cdot 10^6$ s^{-1}. Therefore it is narrowly the globally dominant mode for Model II. The eigenmodes of branch 4 (none of them depicted here) are very similar to those in branch 2 except for slightly shorter axial wavelengths and a phase change in $\tilde{u}_{ze1}$ similar to that of $\tilde{u}_{ye1}$ in figure 5(d).

An important conclusion of this particular study is that global instabilities are not determined exclusively by the intrinsic plasma dynamics but also by the particular set of homogeneous boundary conditions, an aspect out of the capabilities of local stability analyses.

5.2 Model III: Inclusion of zeroth-order electron inertia

Model III considers, as stationary model, the more general Model 0B, instead of the electron-inertialess Model 0A, both being depicted in Fig. 2. The main eigenvalues of the resulting global dispersion relation are shown in figure 11. Branches 1 to 3 are just shifted

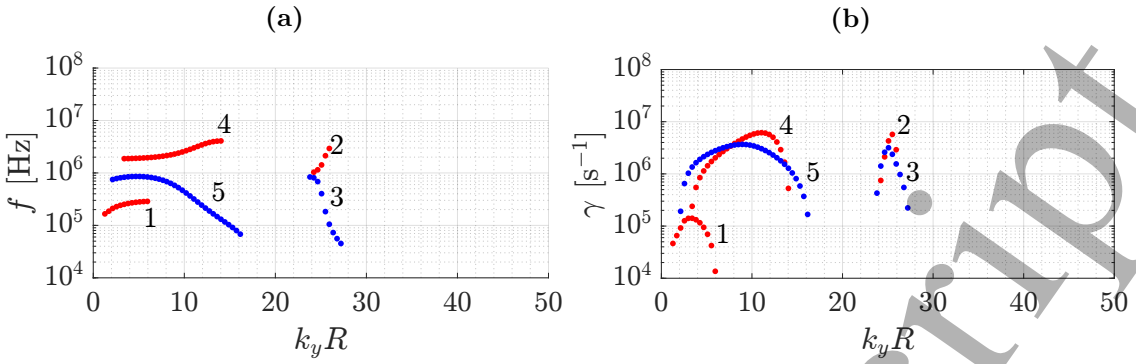

Figure 10: Model II (imposing $\phi_{1N} = 0$). Main eigenvalues. Red and blue colours denote azimuthal propagation in the $+y$ and $-y$ directions, respectively. Branches 4 and 5 are new NPI modes.

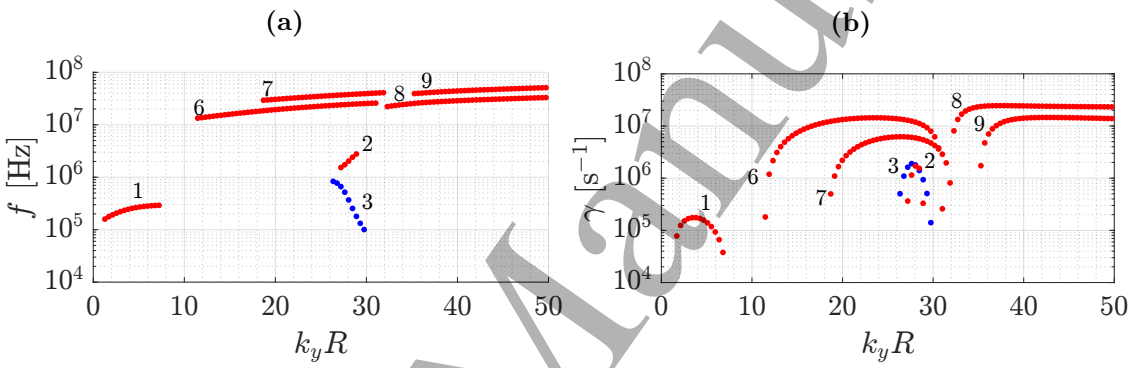

Figure 11: Model III (using the stationary Model 0B). Main eigenvalues. Red and blue colours denote azimuthal propagation along $+y$ and $-y$, respectively. Branches 6 to 9 are new NPI modes.

versions of those of the nominal model in figure 3. Interestingly, the dominant modes in NPI branches 2 and 3 (which counterstream azimuthally) have now very similar growth rates. However, these two branches are now overshadowed by branches 6 to 9, all of NPI type, with significantly higher frequencies. The dominant mode of Model III belongs to branch 8, having $k_yR = 37.4$ and $f = 27.2$ MHz. The eigenmodes are shown in figure 12. However, there are two facts that make not reliable these modes. The first one are the the particular behavior of the instability in the very thin region close to the neutralizer, with very small axial wavelengths. These could be induced by the large values of $\mathrm{d}u_{ye0}/\mathrm{d}z$ there and the boundary conditions at the infinitely thin cathode location. The second one, partially related to the first one, is the failure of the quasineutrality condition, as shown in figure 6(c). Therefore, a consistent stability analysis of Model 0B is going to require considering a finite thickness cathode, the extension to the downstream plume, and the consideration of non-neutral effects in the global perturbation model.

5.3 Model IV: Inclusion of temperature perturbations

This subsection analyzes the effect of allowing perturbations of the electron temperature and the heat flux, i.e. $T_{e1}, q_{ze1} \neq 0$. The system of perturbed equations comprises equa-

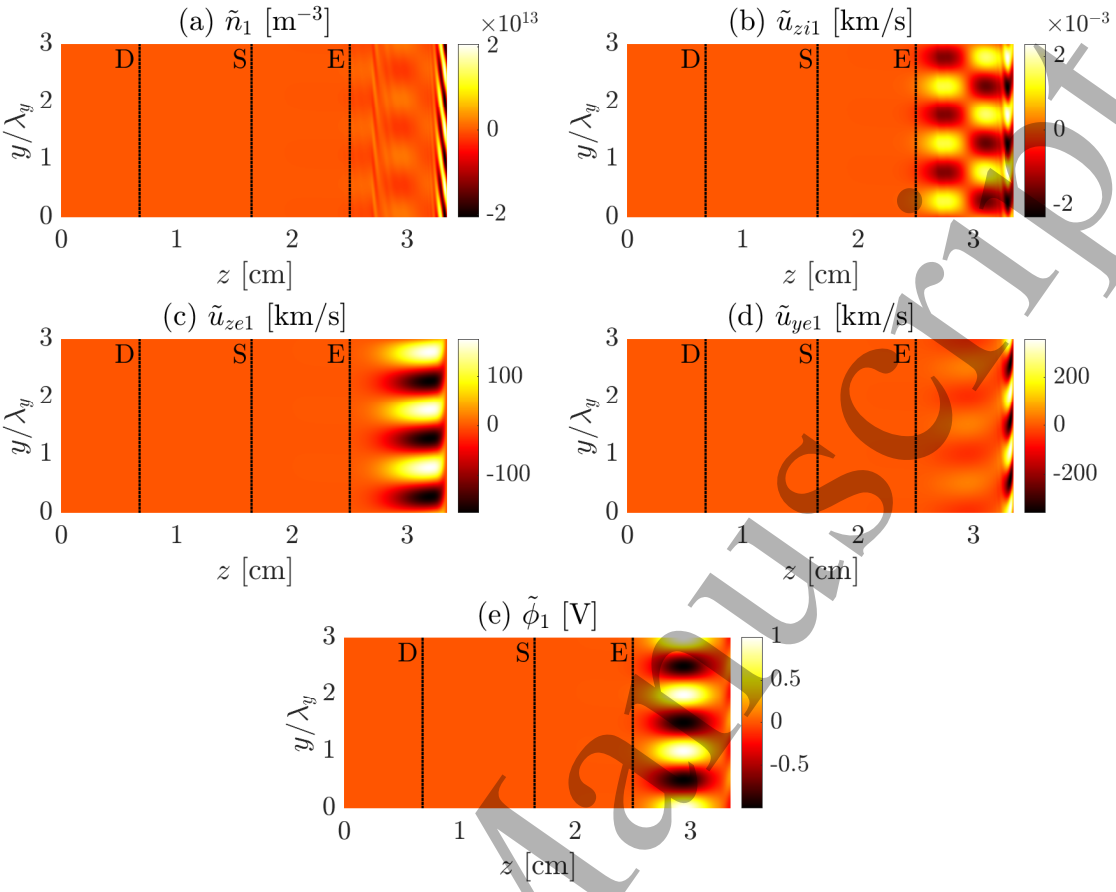

Figure 12: Model III. Instantaneous spatial response for the dominant NPI mode: $k_yR = 37.4$ (i.e. $\lambda_y = 0.71$ cm) and $f = 27.2$ MHz.

tions (30)-(36), with the corresponding boundary conditions. The stationary inertialess Model 0A is used.

The corresponding eigenvalues are represented in Figure 13. The subdominant NAI [in branch 1] and the dominant NPI [in branch 2] modes are still identifiable. There are several new NPI branches [untagged], but the long-term behavior is expected to be dominated, in the near plume, by the dominant NPI mode in branch 2. This branch is unstable within a much wider interval of k_yR and its frequency has increased considerably, up to $f \lesssim 140$ MHz. The fork structure in f with a main and secondary NPI modes has been substituted by a more involved coexistence of instability modes. For instance, now the frequency of the main NPI branch shows a sign change at $k_yR \approx 22$. The dominant NPI mode of Model IV has now $k_yR = 25.1$ and $f = 14.2$ MHz. The corresponding eigenmodes are plotted in figure 14. Compared to the dominant NPI mode of the nominal model (figure 5), this one shows: an attenuation of the fast axial oscillations of $\tilde{u}_{ye1}$, shorter axial wavelengths (i.e., larger k_z) of $\tilde{n}_1$, $\tilde{\phi}_1$ and $\tilde{u}_{zi1}$, and a decrease by one order of magnitude of the relative amplitude of $\tilde{n}_1/\tilde{\phi}_1$. The two last effects lead to an increase of non-neutrality and, indeed, 6(d) shows that non-neutral effects should be included for a correct characterization of the NPI instability with temperature perturbations.

Another feature of Model IV to stand out is that the NAI branch 1 is no more a subdominant mode. This role is taken by branch 10 in figure 13, in particular by the eigenmode

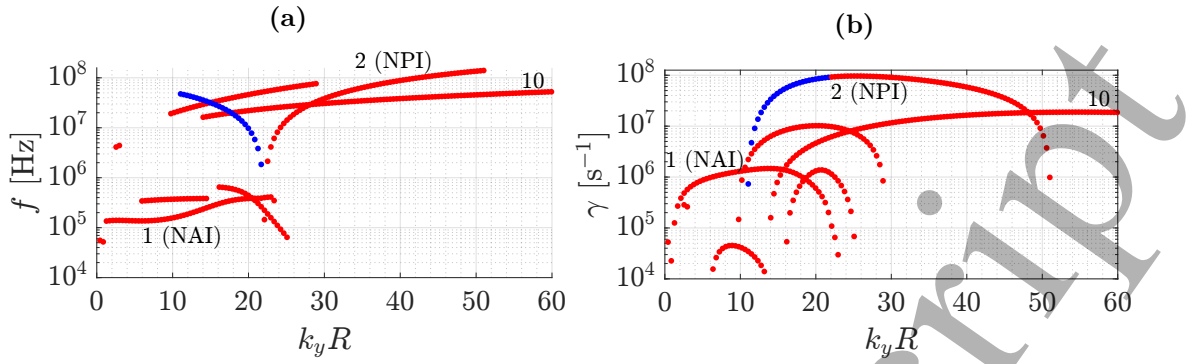

Figure 13: Model IV (allowing temperature perturbations). Main eigenvalues. Red and blue colours denote azimuthal propagation along $+y$ and $-y$, respectively.

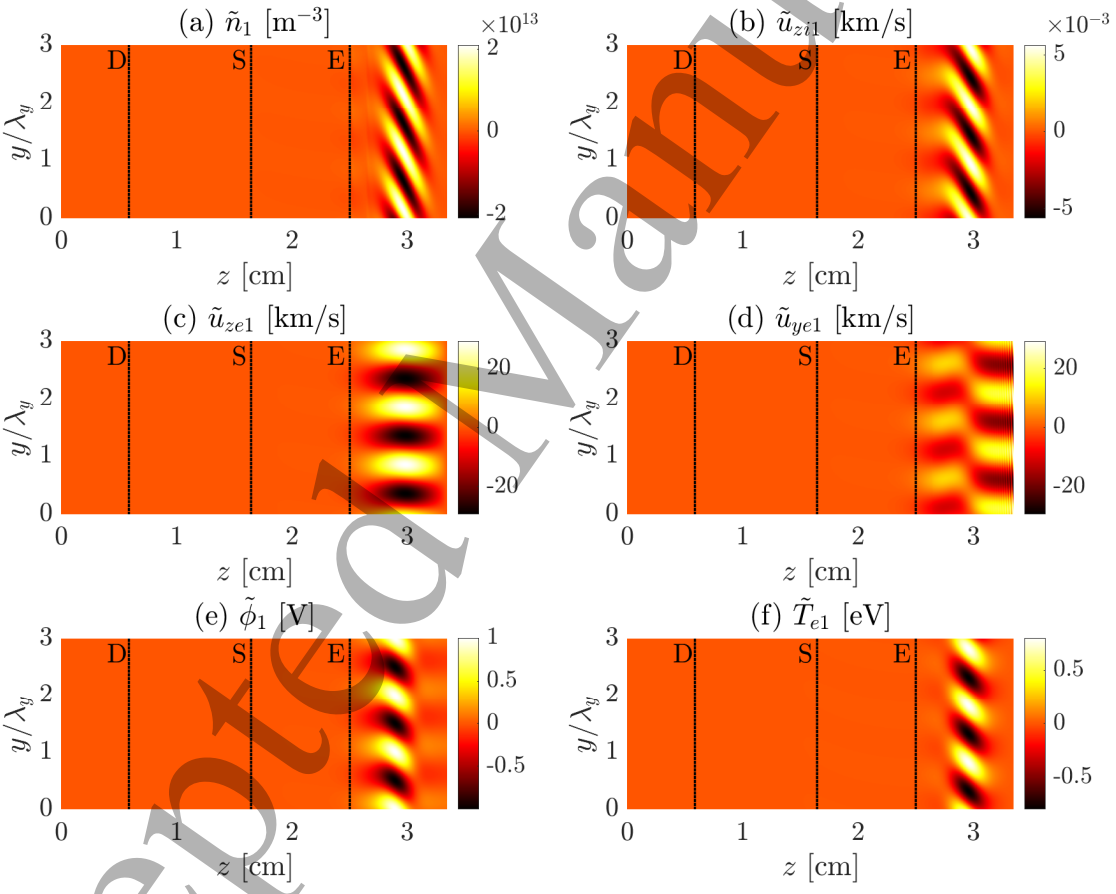

Figure 14: Model IV. Instantaneous spatial response for the dominant NPI mode: $k_yR = 25.1$ and $f = 14.2$ MHz.

with $k_yR = 54.8$ and f =49 Mhz. This mode is not of NAI or NPI type, since it develops between the ion-stagnation point D and the point with n_0 maximum in figure 2(b), i.e in a region with downstream ion flow and $\mathrm{d}n_0/\mathrm{d}z > 0$. This subdominant mode presents significant non-neutral effects too.

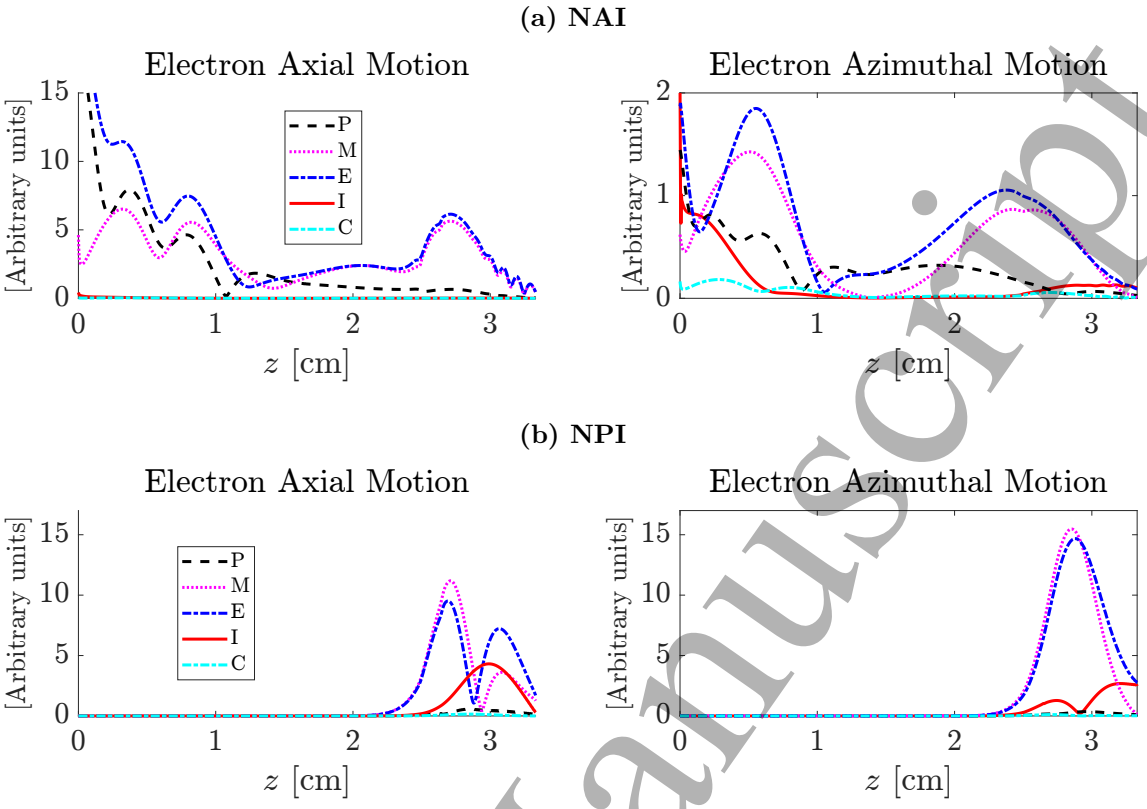

Figure 15: Nominal model. Contributions to the axial and azimuthal components of the first-order electron momentum equations (33) and (34) for the (a) subdominant NAI and (b) dominant NPI modes. P, M, E, I, and C represent pressure, magnetic, electric, inertial, and collisional terms. Complex moduli in arbitrary units are shown. Small-wavelength axial oscillations (mainly due to u_{ye1}) have been filtered out.

6 Analysis of the electron momentum equations

The analysis here is limited to the nominal model.

6.1 Dominant perturbation forces

Equations (33) and (34) for the axial and azimuthal components of the first-order, electron momentum, are analysed in order to identify the main perturbation forces. Figures 15(a) and (b) plot the relative contributions of (I) inertia terms, (P) pressure gradients, (E) electric forces, (M) magnetic forces, and (C) collisional terms, for the subdominant NAI and dominant NPI modes of the nominal model. The first observation is that the electric and magnetic perturbation forces are the main contributions, as expected. The second one is that collisional effects are very marginal for both the NAI and the NPI 'high-frequency' modes (and this is true either keeping or neglecting the turbulent contribution ν_t to the total collision rate ν_e in the perturbation model). Therefore, these two instabilities would pertain to the drift-gradient instability class. Third, the perturbed pressure gradient is totally negligible for the NPI –due to the small (relative) perturbation of plasma density–, but is an important contribution in the inner (subsonic) region of the discharge for the

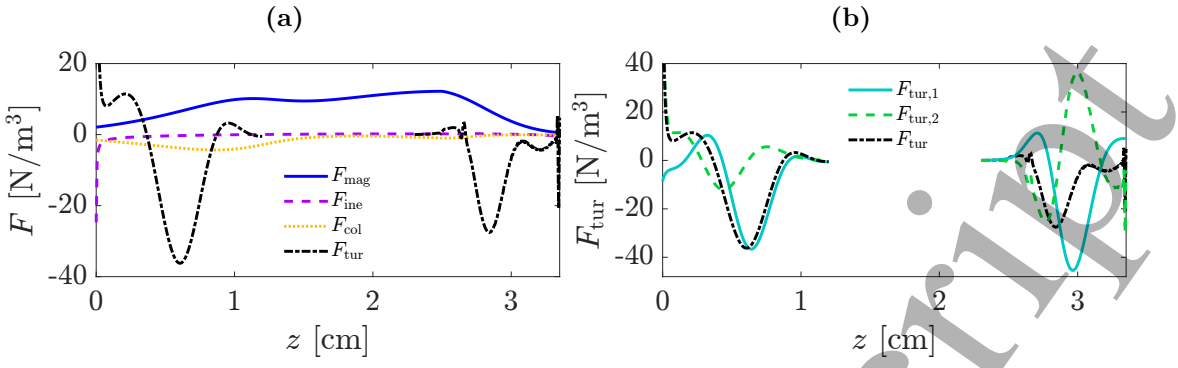

Figure 16: Nominal model. Azimuthal electron momentum balance including turbulent forces. (a) Magnetic force, and turbulent force arising from the dominant NPI mode with $\tilde{\phi}^{NPI}_{1,\max} = 71$V plus the subdominant NAI mode with $\tilde{\phi}^{NAI}_{1,\max} = 10.5$V. (b) Individual contributions of the electric and inertial forces to the previous NPI and NAI turbulent forces. These are proportional to $(\tilde{\phi}^{NPI}_{1,\max})^2$ and $(\tilde{\phi}^{NAI}_{1,\max})^2$, respectively. Small-wavelength axial oscillations (mainly due to u_{ye1}) have been filtered out.

NAI.

Finally, the perturbed inertial forces provide mild local contributions to the azimuthal force balance, in the regions of development of each instability mode, where the stationary azimuthal inertia was already important. In fact, these contributions are partially connected to the fulfilment of the boundary conditions. While in the equilibrium solution only the azimuthal electron inertia has some contribution of interest, in the perturbed NPI modes, the axial electron inertia is as relevant as the azimuthal one. Neglecting smaller contributions, the perturbed electron momentum equations (33) and (34) for the NPI and NAI modes, can be simplified into

$$\mathrm{i}k_y m_e u_{ye0} u_{ze1} \simeq eBu_{ye1} + e\frac{\mathrm{d}\phi_1}{\mathrm{d}z} - \frac{T_{e0}}{n_0}\frac{\mathrm{d}n_1}{\mathrm{d}z}, \tag{45}$$

$$\mathrm{i}k_y m_e u_{ye0} u_{ye1} \simeq -eBu_{ze1} + \mathrm{i}k_y e\phi_1 - \mathrm{i}k_y \frac{T_{e0}}{n_0} n_1, \tag{46}$$

with the (mild) inertial terms are grouped on the left side. The inertia contribution in the perturbed axial equation is of interest only for the NPI since $u_{ze1} = O(u_{ye1})$ (Fig. 5). The pressure terms are only important for the NAI.

6.2 On electron cross-field transport

The quasilinear extension of the fluid model is considered now to analyze quadratically correlated effects of the NPI and NAI modes. The key equation for cross-field electron transport is the stationary azimuthal momentum equation (18), which can be formally expressed as the force balance

$$0 = F_{\rm mag} + F_{\rm ine} + F_{\rm col} + F_{\rm tur}, \tag{47}$$

with $F_{\rm mag} = -eBn_0u_{ze0}$, $F_{\rm ine} = -m_e n_0 u_{ze0}\mathrm{d}u_{ye0}/\mathrm{d}z$, $F_{\rm col} = -m_e(\nu_{e0} - \nu_t)n_0u_{ye0}$, and $F_{\rm tur}$, respectively, the magnetic, inertial, collisional (excluding the empirical contribution of

turbulence), and turbulence-based forces. The magnetic force is undoubtedly the dominant force and must be balanced by the combination of the rest of forces. Figure 16(a) plots $F_{\rm mag}$, $F_{\rm ine}$, and $F_{\rm col}$, and, as expected, inertial and collisional forces cannot balance $F_{\rm mag}$ except at very localized regions. In this case, the compensation comes from the crude and common expression used for the turbulent force, $F_{\rm tur} = -\alpha_t e B n_0 u_{ye0}$, according to Eq. (60).

Let us analyze now, based on the quadratic time-and-azimuth averaged contributions of the dominant NAI and NPI modes, how the resulting azimuthal turbulent force would be. Since the linear perturbation analysis does not predict the saturation level of the instability modes, we will speculate on which saturation levels can lead to $F_{\rm tur}$ balance $F_{\rm mag}$ globally. The time- and azimuth- averaging operator on a quadratic magnitude Φ is defined as

$$\langle \Phi \rangle (z) = \frac{\omega k_y}{4\pi^2} \int_t^{t+2\pi/\omega} {\rm d}t \int_y^{y+2\pi/k_y} {\rm d}y \quad \Phi(t,y,z). \tag{48}$$

For complex, first-order variables $\tilde{\varphi}_1$ and $\tilde{\psi}_1$, fulfilling (13), the correlated product satisfies $\left\langle \tilde{\varphi}_1 \tilde{\psi}_1 \right\rangle = {\rm Re}\{\varphi_1 \psi_1^*\}/2$, with ψ_1^* the complex conjugate of ψ_1.

Departing from Eq. (7), the turbulent force is $F_{\rm tur} = F_{\rm tur,1} + F_{\rm tur,2}$ with

$$F_{\rm tur,1} = -e\langle \tilde{n}_1 \tilde{E}_{y1} \rangle, \tag{49}$$

$$F_{\rm tur,2} = -m_e \left[n_0 \left\langle \tilde{u}_{ze1} \frac{\partial \tilde{u}_{ye1}}{\partial z} \right\rangle + u_{ze0} \left\langle \tilde{n}_1 \frac{\partial \tilde{u}_{ye1}}{\partial z} \right\rangle \right.$$
$$\left. + u_{ye0} \left\langle \tilde{n}_1 \frac{\partial \tilde{u}_{ye1}}{\partial y} \right\rangle + \frac{\partial u_{ye0}}{\partial z} \langle \tilde{n}_1 \tilde{u}_{ze1} \rangle + \left\langle \tilde{n}_1 \frac{\partial \tilde{u}_{ye1}}{\partial t} \right\rangle \right], \tag{50}$$

the contributions from electric and inertial forces, respectively (the pressure azimuthal gradient does not contribute, on average, to turbulent transport because of its azimuthal periodicity).

The shapes of $F_{\rm tur}(z)$ generated by the dominant NPI and the subdominant NAI modes are depicted in Figure 16 (a) too. The contributions are proportional to $(\tilde{\phi}^{NPI}_{1,\max})^2$ and $(\tilde{\phi}^{NAI}_{1,\max})^2$, respectively for each mode. As commented above, the saturation values of the electric potential, $\tilde{\phi}^{NPI}_{1,\max}$ and $\tilde{\phi}^{NAI}_{1,\max}$, are out of reach of the linear model, and those selected for the plots, $\tilde{\phi}^{NPI}_{1,\max} = 71$V and $\tilde{\phi}^{NAI}_{1,\max} = 10.5$V, correspond just to those making $F_{\rm tur}$ to compensate globally $F_{\rm mag}$ in the last and first centimeter of the domain, where, respectively, the NPI and NAI are significant. The associated amplitudes of the azimuthal electric fields are $\tilde{E}_{y1,\max} = {\rm Re}\{{\rm i}k_y \phi_{1,\max}\}$ are 390 V/cm and 7.4 V/cm for the NPI and NAI modes, respectively. These magnitudes of the perturbations fields are comparable to those of the local zeroth-order electric field, thus suggesting that the NPI and NAI modes must develop well into the nonlinear regime in order to contribute to the cross-field transport.

Figure 16(b) depicts the electric and inertial contributions to $F_{\rm tur}$. The inertial contribution, $F_{\rm tur,2}$, is small for the NAI, but it is of the same order than the electric one, $F_{\rm tur,1}$, for the NPI. This result is not immediate since, within first order, electron inertia ($m_e u_{ye0} u_{ye1}$) is generally small compared to the electric force ($e\phi_1$). However, for the second-order forces,

$$\frac{m_e n_0 u_{ze1} \partial u_{ye1}/\partial z}{e k_y n_1 \phi_1} \sim \frac{m_e u_{ye0} u_{ye1}}{e\phi_1} \cdot \frac{n_0 u_{ze1}}{n_1 u_{ye0}} \geq O(1), \tag{51}$$

since $n_0 u_{ze1}/n_1 u_{ye0} \sim 100$ for the NPI (as for the quasineutrality condition, the extremely low n_1 disrupts the expected natural orderings). This, and a mildly higher correlation level on the electric force, explain that $F_{\text{tur},2} \sim F_{\text{tur},1}$ for the NPI.

Next, while $\int_{z_A}^{z_N} F_{\text{tur}} \mathrm{d}z < 0$, is negative (and, thus, contributes positively to cross-field transport), the profile of $F_{\text{tur}}(z)$ is very rippled spatially, F_{tur} becoming even positive in certain subregions. This is natural to the oscillatory character of modes generating F_{tur} but is far different from the gentle profile of $F_{\text{tur}} = -\alpha_t e B n_0 u_{ye0}$, used to construct the equilibrium solution (although this one could be interpreted as a spatially-averaged force). An iterative scheme can be set up to obtain a solution consistent with the rippled $F_{\text{tur}}(z)$ up to second order. This is out of the scope of this work and a challenging problem anyway. A spatially rippled $F_{\text{tur}}(z)$ enhances the relevance of the electron inertia force in the equilibrium solution, since it is the first term reacting to variations of $F_{\text{tur}}(z)$, and likely leads to some rippling in the rest of plasma variables at equilibrium and to changes in the linear perturbation modes. Furthermore, the non-negligible role of electron inertia in the instability analysis here, implies that gyroviscous effects, of the same order than inertia effects in the standard finite-Larmor-radius ordering [39, 23], should be included in the model to strengthen its consistency. But the gyroviscous tensor introduces second-order axial derivatives, implying a major change in the mathematical formulation, which here is first-order in axial derivatives.

To conclude it is worth observing that a spatially rippled $F_{\text{tur}}(z)$ is also found in the nonlinear kinetic simulations of a HET discharge [25], although instabilities there were attributed to kinetic electron-drift instabilities. A fully non-linear fluid model would be needed to a more solid comparison of kinetic and fluid contributions to cross-field transport.

7 Summary and conclusions

The plasma discharge in a HET from the anode to the external cathode is highly inhomogeneous, so the linear stability analysis of a stationary response must consider the discharge globally. Departing from a fluid model of the discharge that ignores the radial direction, and is quasineutral except for the anode sheath, a perturbation scheme is applied to define (i) a zeroth-order axisymmetric stationary axial model plus (ii) a first-order model of small perturbations. Both pressure effects and electron inertia effects are kept in the two models, with the interest of assessing their relevance.

Fourier transforms are applied only in time and the azimuthal direction, so the perturbation model constitutes a set of ordinary differential equations in z for each azimuthal wavenumber k_y and frequency ω. The stability analysis of the perturbation model considers homogeneous boundary conditions at the anode, the cathode, and the internal sonic point. Given k_y, the problem admits non-trivial solutions only at specific values of ω. A discretization method in a uniform grid has been implemented to transform the differential Sturm-Liouville problem into an algebraic eigenvalue problem. For each real k_y, complex eigenvalues ω are found; the corresponding eigenvectors build up the perturbation solution.

The analysis is focused in the mid-to-high frequency range (say, $f > 100$ kHz) and high-wavenumber range (i.e. $k_y R$ large) but still within the fluid-formulation validity range. Two well-distinguished instability types are found under a broad range of conditions. There is first a dominant instability mode (NPI) developing in the near-plume. It has frequencies in the ranges $f \sim$ 1-30 MHz and azimuthal mode numbers $k_y R \sim$ 10-40. It involves electron perturbations almost exclusively and travels in the $+u_{ye0}$ direction. By

modifying $B(z)$ it is shown that the NPI development is related to the region where $\mathrm{d}B/\mathrm{d}z$ is negative, thus suggesting that the NPI could be related to the classical drift-gradient instability of Esipchuk and Tilinin. There is, then, a subdominant instability mode (NAI) developing mainly near the anode. This mode has lower frequencies ($f \sim$ 100-300 kHz) and mode numbers ($k_y R \sim$ 1-10) and involves both perturbations of electrons and ions. This mode could be a high-frequency manifestation of a rotating spoke.

For the nominal model (the main one studied here) there is a second counterstreaming NPI branch (i.e. travelling along $-u_{ye0}$) which could be related to some experimental observations but it is never dominant in the analyses here. For a short channel or a certain anode-to-cathode electric connection, a second pair of NPI branches develop at lower wavenumbers, and one of their modes can even become the dominant mode. When zeroth-order electron inertia (mostly significant close to the anode and cathode boundaries) or electron temperature perturbations are included in the analysis, the number of unstable eigenvalue branches of the dispersion relation increase much, and the discussion is more involved. Still, there is a dominant NPI mode but mode number and frequency have shifted to higher values.

Both NPI and NAI are not simple normal waves since, for each k_y and ω, a fast Fourier transform shows that different axial wavenumbers k_z characterize the propagation of the different plasma variables, which means that the oblique propagation is different for each of them, contrary to local analyses based on setting both wavenumbers, and obtaining $\omega(k_y, k_z)$. The two perturbation modes are nearly collisionless, pressure effects matter only for the NAI (developing in the subsonic region of the plasma beam), and first-order electron inertia is a small correction to them. Quasineutrality is satisfied by the NAI but not always by the NPI: non-neutral effects appear, even with $k\lambda_D \ll 1$, due to the very low perturbations of the ions in the NPI.

The last part of the paper has been devoted to a speculative analysis on the possible contribution of the NPI and the NAI to the electron cross-field transport, through quadratically-correlated electric and inertia forces. The conclusions have been that: (1) a fully nonlinear development of the modes is required to obtain a significant turbulent azimuthal force, (2) the contribution of electron inertia to the net turbulent force is not small for the NPI (because of the small density perturbation and the resulting quadratic electric force), and (3) the turbulent force is highly rippled axially.

This last feature has important consequences on the stationary mathematical model. First, it makes electron inertia a key mechanism to control spatial rippling on the equilibrium solution. Second, the gyroviscous effects, cannot be further ignored, mainly if dealing with a rippled solution, but these imply major changes to the present first-order mathematical formulation. Finally, since the NPI develops close to the cathode boundary, the extension of the global discharge model beyond the cathode, into the current-free plume, is another interesting direction of research.

Acknowledgements

This research was funded by the Comunidad de Madrid (Spain), under PROMETEO-CM project, with grant number Y2018/NMT-4750. Enrique Bello-Benítez is supported by Spain's Ministerio de Ciencia, Innovación y Universidades, under grant FPU18/03686. The authors acknowledge useful discussions on this work with J. J. Ramos and P. Fajardo.

A Expressions for collision-related parameters

This Appendix compiles the expressions for the collision-related terms of Eqs. (2)-(9) and the values selected in the simulations for some of the constants. The expressions come from previous papers on the same model by Ahedo and coworkers.

The ionization or production frequency, ν_p, is modeled as $\nu_p = n_n \bar{c}_e \bar{\sigma}_{\rm ion}$, with

$$\bar{\sigma}_{\rm ion} = \sigma_{\rm ion,0} \left[1 + \frac{T_e E_{\rm ion}}{(T_e + E_{\rm ion})^2}\right] \exp\left(-\frac{E_{\rm ion}}{T_e}\right) \tag{52}$$

where $E_{\rm ion}$ stands for the primary ionization energy. For xenon: $E_{\rm ion} = 12.1$ eV, $\sigma_{\rm ion,0} = 5 \times 10^{-20}$ m^2. The effective energy loss due to ionization, $E_{\rm inel}$, satisfies

$$\frac{E_{\rm inel}}{E_{\rm ion}} = 2 + \frac{1}{4} \exp\left(\frac{2E_{\rm ion}}{3T_e}\right) \tag{53}$$

The elastic electron-neutral collisions frequency is $\nu_{en} = n_n \bar{c}_e \sigma_{en}$. Here, and for xenon the cross-section σ_{en} is taken approximately constant and equal to $\sigma_{en} = 27 \times 10^{-20}$ m^2.

The electron-ion (Coulomb) collision frequency is $\nu_{ei} = n R_{ei}$, with R_{ei} given by

$$\frac{R_{ei}}{10^{-12}\mathrm{m^3 s^{-1}}} = 2.9 \cdot \left(\frac{1\ \mathrm{eV}}{T_e}\right)^{3/2} \ln\Lambda \quad \text{and} \quad \ln\Lambda \approx 9 + \frac{1}{2}\ln\left[\left(\frac{10^{18}\ \mathrm{m^{-3}}}{n_e}\right)\left(\frac{T_e}{1\ \mathrm{eV}}\right)^3\right]. \tag{54}$$

The ion-neutral (charge-exchange) collision frequency is $\nu_{in} = n_n c_{in} \sigma_{in}$, with $c_{in} = |u_{zi} - u_{zn}|$ and

$$\sigma_{in} = \sigma_{in0}\left[1 - 0.2 \log_{10} \frac{c_{in}}{1\ \mathrm{km/s}}\right]^2 \tag{55}$$

and $\sigma_{in0} = 81 \cdot 10^{-20}$ m^2 for Xe.

The wall-loss frequency of particles is

$$\nu_w = \tilde{\nu}_w \frac{2\pi R}{A_c} c_s \tag{56}$$

with $\tilde{\nu}_w$ a constant (accounting for plasma density decrease near the wall); $\tilde{\nu}_w = 0.17$ is used here. The effective axial velocity of wall-born neutrals from ion recombination is

$$u_{znw} = a_w u_{zn} + (1 - a_w) u_{zi} \tag{57}$$

where a_w is a velocity accommodation factor; $a_w = 0.85$ is used here. The wall-loss frequency for momentum and energy are $\nu_{wm} = \beta_m \nu_w$ and $\nu_{we} = \beta_e \nu_w$, respectively with

$$\beta_m = \frac{\delta_w}{1 - \delta_w}, \qquad \beta_e = 5.62 + \frac{1.65}{1 - \delta_w}. \tag{58}$$

Here, δ_w is the effective secondary electron emission yield from the wall, which is modeled as

$$\delta_w(T_e) = \sqrt{T_e/T_1} \quad \text{if} \quad T_e < T_e^* \tag{59}$$

and $\delta_w = \delta_w^* = \sqrt{T_e^*/T_1}$ if $T_e \geq T_e^*$, where T_1 is the temperature leading (theoretically) to a 100% yield (which depends on the wall material) and T_e^* is the temperature where the

charge-saturation limit is reached at the wall. Here: $T_e^*/T_1 = 0.967$, $\delta_w^* = 0.983$, and $T_1 = 37$ eV.

Turbulent transport in the stationary solution is introduced through an effective collisional frequency

$$\nu_t = \alpha_t \omega_{ce} \tag{60}$$

with α_t a constant equal to 0.0094 in the simulations here.

B Symmetry of the perturbation problem

As noted in the main text, the parametric region with $k_y < 0$ yields the same perturbation modes than those obtained for $k_y > 0$. Analytical evidence is provided here by, first, proving that the perturbation problem satisfies the symmetry condition

$$\omega_r(-k_y) = -\omega_r(k_y), \quad \gamma(-k_y) = \gamma(k_y), \quad \varphi_1(z, -k_y, -\omega^*) = \varphi_1^*(z, k_y, \omega), \tag{61}$$

for every first-order variable φ_1, with the asterisk denoting the complex conjugate. The solutions, for k_y and $-k_y$, complying with (61) do not generally belong to the same branch (meaning by 'branch' the continuous curves in, e.g., figure 3).

According to the symmetry condition (61), every perturbation equation, that can be expressed as $f(k_y, \omega, \boldsymbol{\varphi}_1) = 0$ (being $\boldsymbol{\varphi}_1$ the vector of first-order variables), complies with

$$f^*(k_y, \omega, \boldsymbol{\varphi}_1) = f(-k_y, -\omega^*, \boldsymbol{\varphi}_1^*). \tag{62}$$

In that case, if there exists a solution for k_y, ω and $\boldsymbol{\varphi}_1$ obeying $f(k_y, \omega, \boldsymbol{\varphi}_1) = 0$; there must exist another solution fulfilling $f(-k_y, -\omega^*, \boldsymbol{\varphi}_1^*) = 0$ for $-k_y$, $-\omega^*$ and $\boldsymbol{\varphi}_1^*$. Let us now demonstrate that (62) is satisfied by the perturbation equations (30)-(36). It is enough with providing proof for electron-related equations, since those for ions are simplified versions of these. Also, for the sake of conciseness, we will work on the case with $T_{e1} = 0$; but the property (62) remains valid for the more general case with non-zero T_{e1} and q_{ze1}.

If k_y, ω and $\boldsymbol{\varphi}_1$ are substituted by $-k_y$, $-\omega^*$ and $\boldsymbol{\varphi}_1^*$ in the first-order electron continuity equation (31), the result is

$$u_{ze0}\frac{\mathrm{d}n_1^*}{\mathrm{d}z} + n_0\frac{\mathrm{d}u_{ze1}^*}{\mathrm{d}z} = \left(-\mathrm{i}\omega^* + \mathrm{i}k_y u_{ye0} - \frac{\mathrm{d}u_{ze0}}{\mathrm{d}z} + \nu_p - \nu_w\right) n_1^* - \frac{\mathrm{d}n_0}{\mathrm{d}z}u_{ze1}^* + \mathrm{i}k_y n_0 u_{ye1}^*, \tag{63}$$

that can be easily proved to be equal to the complex conjugate of equation (31), thus fulfilling (62). Similarly, the same substituion for the electron momentum equations (33) and (34), yields

$$u_{ze0}\frac{\mathrm{d}u_{ze1}^*}{\mathrm{d}z} + \frac{T_{e0}}{m_e n_0}\frac{\mathrm{d}n_1^*}{\mathrm{d}z} - \frac{e}{m_e}\frac{\mathrm{d}\phi_1^*}{\mathrm{d}z} = \left(-\mathrm{i}\omega^* + \mathrm{i}k_y u_{ye0} - \frac{\mathrm{d}u_{ze0}}{\mathrm{d}z} - \nu_e\right) u_{ze1}^* + \frac{eB}{m_e}u_{ye1}^* + \frac{T_{e0}}{m_e n_0^2}\frac{\mathrm{d}n_0}{\mathrm{d}z}n_1^*, \tag{64}$$

$$u_{ze0}\frac{\mathrm{d}u_{ye1}^*}{\mathrm{d}z} = \left(-\mathrm{i}\omega^* + \mathrm{i}k_y u_{ye0} - \nu_e\right) u_{ye1}^* - \left(\frac{\mathrm{d}u_{ye0}}{\mathrm{d}z} + \frac{eB}{m_e}\right) u_{ze1}^* + \mathrm{i}k_y\frac{T_{e0}}{m_e n_0}n_1^* - \mathrm{i}k_y\frac{e}{m_e}\phi_1^*, \tag{65}$$

which are equal to complex conjugate of equations (33) and (34), respectively. The same procedure can be followed to demonstrate the compliance with (62) of the general system with non-zero T_{e1} and q_{ze1}; and including electron energy and heat flow equations.

Following the definition (13), for every complex perturbation solution, only the real part has physical meaning. It happens that the modes satisfying the proposed symmetry also fulfill

$$\tilde{\varphi}_1(z,y,t) = \mathrm{Re}\{\varphi_1(z,k_y,\omega)\exp\left(-\mathrm{i}\omega t + \mathrm{i}k_y y\right)\} = \mathrm{Re}\{\varphi_1^*(z,k_y,\omega)\exp\left(\mathrm{i}\omega^* t - \mathrm{i}k_y y\right)\} \quad (66)$$

and, thus, they are the same mode.

C Numerical method for the perturbation problem

The system of linearized macroscopic equations can be written formally as a general homogeneous system of ordinary differential equations

$$\bar{\mathbf{A}} \cdot \frac{\mathrm{d}\boldsymbol{x}_1}{\mathrm{d}z} = \left(\bar{\mathbf{B}} + \mathrm{i}\omega\bar{\mathbf{C}} + \mathrm{i}k_y\bar{\mathbf{D}} + k_y^2\bar{\mathbf{D}}_2\right)\cdot\boldsymbol{x}_1 \quad (67)$$

with $\boldsymbol{x}_1 = \boldsymbol{x}_1(z)$ being the vector of perturbation variables and having length m, say. The coefficients of matrices $\bar{\mathbf{A}}$, $\bar{\mathbf{B}}$, $\bar{\mathbf{C}}$, $\bar{\mathbf{D}}$ and $\bar{\mathbf{D}}_2$ are functions of just z and the equilibrium solution $\boldsymbol{x}_0 = \boldsymbol{x}_0(z)$. Similarly, each boundary condition of the problem is homogeneous and can be expressed as a linear combination of the perturbation variables at the corresponding point of application (since the boundary conditions do not involve axial gradients).

The global linear stability problem, or Sturm-Liouville problem, described by equation (67) and its set of homogeneous boundary conditions consists of finding non-trivial solutions $\boldsymbol{x}_1(z)$ (eigenfunctions) at specific values of the complex frequency ω (eigenvalues) for given k_y and background plasma state $\boldsymbol{x}_0(z)$.

Equation (67) is solved in a discrete way on an uniform grid with p points covering the distance from the anode sheath edge (B) to the neutralizer (N). The unknowns of the discrete problem, $\boldsymbol{X}_1$, are the values of the first order variables, $\boldsymbol{x}_1$, at the grid points. Let j be the index, going from 1 to p, denoting the grid point. This means a total of mp unknowns, which satisfy m boundary conditions and $m\,(p-1)$ macroscopic equations. These come from evaluating equations (67) at p different axial positions of the domain. These do not need to coincide with the grid points. After checking different possibilities to proceed, the method identified as the most numerically robust has been selected.

This method evaluates the first-order system (67) at intermediate points in between grid points; the non-integer index $j+1/2$ denotes the midpoint between grid points j and $j+1$. This directly yields $m(p-1)$ equations, which can be written, analogously to equation (67), as the system

$$\bar{\mathbf{A}}_g \cdot \frac{\mathrm{d}\boldsymbol{X}_1^*}{\mathrm{d}z} = \left(\bar{\mathbf{B}}_g + \mathrm{i}\omega\bar{\mathbf{C}}_g + \mathrm{i}k_y\bar{\mathbf{D}}_g + k_y^2\bar{\mathbf{D}}_{2,g}\right)\cdot\boldsymbol{X}_1^* \quad (68)$$

where $\boldsymbol{X}_1^*$ stands for the vector of first order quantities at midpoints, which is $m(p-1)$ elements long. The matrices in the previous expression are squared with column length $m(p-1)$, and are global versions of those in equation (67). Their coefficients come from evaluating the local matrices at each midpoint. The specific arrangement of these coefficients within global matrices depends on the order used for the elements in vector $\boldsymbol{X}_1^*$.

Equation (68) has to be expressed in terms of the unknown vector $\boldsymbol{X}_1$. First, the derivatives at midpoints (collected in $\mathrm{d}\boldsymbol{X}_1^*/\mathrm{d}z$) are estimated, using grid-point values, with the centered finite difference formula

$$\left.\frac{\mathrm{d}\boldsymbol{x}_1}{\mathrm{d}z}\right|^{j+1/2} \approx \frac{\boldsymbol{x}_1^{j+1} - \boldsymbol{x}_1^{j}}{\Delta z} \tag{69}$$

where Δz is the grid step. Using this equation it is possible to build a finite difference matrix $\bar{\mathbf{F}}$ such that

$$\frac{\mathrm{d}\boldsymbol{X}_1^*}{\mathrm{d}z} \approx \bar{\mathbf{F}} \cdot \boldsymbol{X}_1. \tag{70}$$

Second, the values of perturbations at midpoints (collected in $\boldsymbol{X}_1^*$) can be estimated as the mean of the values at the two nearest grid points, i.e

$$\boldsymbol{x}_1^{j+1/2} \approx \frac{\boldsymbol{x}_1^{j} + \boldsymbol{x}_1^{j+1}}{2} \tag{71}$$

This expression can be used to build an averaging matrix $\bar{\mathbf{M}}$ such that $\boldsymbol{X}_1^* \approx \bar{\mathbf{M}} \cdot \boldsymbol{X}_1$. The size of matrices $\bar{\mathbf{F}}$ and $\bar{\mathbf{M}}$ is $m(p-1) \times mp$.

Using these discretizations in equation (68) yields the algebraic equation

$$\bar{\mathbf{A}}_g \cdot \bar{\mathbf{F}} \cdot \boldsymbol{X}_1 = \left(\bar{\mathbf{B}}_g + \mathrm{i}\omega\bar{\mathbf{C}}_g + \mathrm{i}k_y\bar{\mathbf{D}}_g + k_y^2\bar{\mathbf{D}}_{2,g}\right) \cdot \bar{\mathbf{M}} \cdot \boldsymbol{X}_1 \tag{72}$$

The size of the matrices multiplying $\boldsymbol{X}_1$ is $m(p-1) \times mp$. The set of linear homogeneous boundary conditions can be expressed as linear combinations of the the discrete unknowns of the problem in the form $\bar{\mathbf{G}} \cdot \boldsymbol{X}_1 = \mathbf{0}$.

Then, the complete discrete system of equations that gives an approximate solution to the Sturm-Liouville problem of equation (67) reads

$$\left[\begin{pmatrix} \bar{\mathbf{A}}_g \cdot \bar{\mathbf{F}} - \left(\bar{\mathbf{B}}_g + \mathrm{i}k_y\bar{\mathbf{D}}_g + k_y^2\bar{\mathbf{D}}_{2,g}\right) \cdot \bar{\mathbf{M}} \\ \bar{\mathbf{G}} \end{pmatrix} - \begin{pmatrix} \bar{\mathbf{C}} \cdot \bar{\mathbf{M}} \\ \bar{\mathbf{0}} \end{pmatrix} \mathrm{i}\omega\right] \cdot \boldsymbol{X}_1 = \mathbf{0} \tag{73}$$

This is a generalized algebraic eigenvalue problem with ω and the corresponding $\boldsymbol{X}_1$ being the eigenvalues and eigenvectors, respectively. Once solved, the axial evolution of the perturbation plasma variables is obtained in the complex plane.

This scheme has shown good numerical convergence and, for simple equilibrium solutions, the discrete solution has been verified with analytical solutions. An alternative discretization scheme would have been to evaluate the first order fluid equations at grid points (instead of at midpoints) and use forward, centered, and backward finite difference schemes for estimating axial gradients at left boundary, interior points and right boundary, respectively. However, the complete system (67) cannot be evaluated at every grid point, since this would provide mp equations, and m boundary conditions should still be added. This implies that m fluid equations must be disregarded, but that selection is not at all trivial when boundary conditions are set at different points (B, S and N).

References

[1] E. Choueiri. Plasma oscillations in Hall thrusters. Physics of Plasmas, 8(4):1411–1426, 2001.

[2] G.S. Janes and R.S. Lowder. Anomalous electron diffusion and ion acceleration in a low-density plasma. Physics of Fluids, 9(6):1115–1123, 1966.

[3] J.P. Boeuf. Tutorial: Physics and modeling of Hall thrusters. J. Applied Physics, 121(1):011101, 2017.

[4] D.W. Forslund, R.L. Morse, and C.W. Nielson. Electron cyclotron drift instability. Physical Review Letters, 25:1266–1270, 1970.

[5] A. Ducrocq, J.C. Adam, A. Héron, and G. Laval. High-frequency electron drift instability in the cross-field configuration of Hall thrusters. Physics of Plasmas, 13:102111, 2006.

[6] J. Cavalier, N. Lemoine, G. Bonhomme, S. Tsikata, C. Honoré, and D. Grésillon. Hall thruster plasma fluctuations identified as the E×B electron drift instability: Modeling and fitting on experimental data. Physics of Plasmas, 20(8):082107, 2013.

[7] S. Janhunen, A. Smolyakov, O. Chapurin, D. Sydorenko, I. Kaganovich, and Y. Raitses. Nonlinear structures and anomalous transport in partially magnetized ExB plasmas. Physics of Plasmas, 25:11608, 2018.

[8] N. A. Krall and P. C. Liewer. Low-frequency instabilities in magnetic pulses. Physical Review A, 4:2094–2103, 1971.

[9] J.B. McBride, E. Ott, J.P. Boris, and J.H. Orens. Theory and simulation of turbulent heating by the modified two-stream instability. The Physics of Fluids, 15(12):2367–2383, 1972.

[10] S. Janhunen, A. Smolyakov, D. Sydorenko, M. Jimenez, I. Kaganovich, and Y. Raitses. Evolution of the electron cyclotron drift instability in two-dimensions. Physics of Plasmas, 25(8):082308, 2018.

[11] E. Ahedo, J.M. Gallardo, and M. Martínez-Sánchez. Effects of the radial-plasma wall interaction on the axial Hall thruster discharge. Physics of Plasmas, 10(8):3397–3409, 2003.

[12] E. Ahedo and D. Escobar. Influence of design and operation parameters on Hall thruster performances. Journal of Applied Physics, 96(2):983–992, 2004.

[13] D. Escobar and E. Ahedo. Low frequency azimuthal stability of the ionization region of the Hall thruster discharge. II. Global analysis. Physics of Plasmas, 22:102114, 2015.

[14] D. Escobar and E. Ahedo. Numerical analysis of high-frequency azimuthal oscillations in Hall thrusters. In 34^{th} International Electric Propulsion Conference, number IEPC-2015-371, Hyogo-Kobe, Japan, July 6-10, 2015. Electric Rocket Propulsion Society.

[15] D. Escobar and E. Ahedo. Low frequency azimuthal stability of the ionization region of the Hall thruster discharge. I. Local analysis. Physics of Plasmas, 21(4):043505, 2014.

[16] A.A. Litvak and N.J. Fisch. Rayleigh instability in Hall thrusters. Physics of Plasmas, 11:1379, 2004.

[17] A. Kapulkin, J. Ashkenazy, A. Kogan, G. Appelbaum, D. Alkalay, and M. Guelman. Electron instabilities in Hall thrusters: Modeling and application to electric field

diagnostics. In Proceedings of the 28th International Electric Propulsion Conference, 2003.

[18] A. Kapulkin and M. Guelman. Lower-hybrid instability in Hall thruster. In Proceedings of the 29th International Electric Propulsion Conference, IEPC-2005-88, 2005.

[19] E. A. Sorokina, N. A. Marusov, V. P. Lakhin, and V. I. Ilgisonis. Discharge oscillations in Morozov's stationary plasma thruster as a manifestation of large-scale modes of gradient drift instability. Plasma Physics Reports, 45(1):1, 2019.

[20] N. A. Marusov, E. A. Sorokina, V. I. Ilgisonis, and V. P. Lakhin. Large-scale azimuthal structures in Hall-type plasma discharges. Physics of Plasmas, 26(9):090701, 2019.

[21] I. Romadanov, A.I. Smolyakov, Y. Raitses, I.D. Kaganovich, T. Tian, and S. Ryzhkov. Structure of nonlocal gradient-drift instabilities in hall exb discharges. Physics of Plasmas, 23:122111, 2016.

[22] W. Frias, A.I. Smolyakov, I.D. Kaganovich, and Y. Raitses. Long wavelength gradient drift instability in Hall plasma devices. I. Fluid theory. Physics of Plasmas, 19:072112, 2012.

[23] A.I. Smolyakov, O. Chapurin, W. Frias, O. Koshkarov, I. Romadanov, T. Tang, M. Umansky, Y. Raitses, I.D. Kaganovich, and V.P. Lakhin. Fluid theory and simulations of instabilities, turbulent transport and coherent structures in partially-magnetized plasmas of ExB discharges. Plasma Physics and Controlled Fusion, 59:014041, 2017.

[24] J.C. Adam, A. Herón, and G. Laval. Study of stationary plasma thrusters using two-dimensional fully kinetic simulations. Physics of Plasmas, 11:295–305, 2004.

[25] T. Lafleur and P. Chabert. The role of instability-enhanced friction on 'anomalous' electron and ion transport in Hall-effect thrusters. Plasma Sources Science and Technology, 27:015003, 2017.

[26] T. Charoy, T. Lafleur, A. Tavant, P. Chabert, and A. Bourdon. A comparison between kinetic theory and particle-in-cell simulations of anomalous electron transport in ExB plasma discharges. Physics of Plasmas, 27(6):063510, 2020.

[27] A.A. Litvak and N.J. Fisch. Resistive instabilities in Hall current plasma discharge. Physics of Plasmas, 8(2):648–651, 2001.

[28] V. P. Lakhin, V. I. Ilgisonis, A. I. Smolyakov, E. A. Sorokina, and N. A. Marusov. Effects of finite electron temperature on gradient drift instabilities in partially magnetized plasmas. Physics of Plasmas, 25:012106, 2018.

[29] E. Ahedo, J.M. Gallardo, and M. Martínez-Sánchez. Model of the plasma discharge in a Hall thruster with heat conduction. Physics of Plasmas, 9(9):4061–4070, 2002.

[30] E. Ahedo, P. Martínez-Cerezo, and M. Martínez-Sánchez. One-dimensional model of the plasma flow in a Hall thruster. Physics of Plasmas, 8:3058–3068, 2001.

[31] Y.V. Esipchuk and G.N. Tilinin. Drift instability in a Hall-current plasma accelerator. Sov. Physics-Tech. Physics, 21(4):417–423, 1976.

[32] E. Ahedo, P. Martínez-Cerezo, and M. Martínez-Sánchez. Steady and linearly-unsteady analysis of a Hall thruster with an internal sonic point. In Proc. 36th

Joint Propulsion Conference, Huntsville, AL, AIAA 2000-3655. American Institute of Aeronautics and Astronautics, 2000.

[33] N A Marusov, E A Sorokina, V P Lakhin, V I Ilgisonis, and A I Smolyakov. Gradient-drift instability applied to Hall thrusters. Plasma Sources Science and Technology, 28(1):015002, 2019.

[34] M. S. McDonald and A. D. Gallimore. Rotating spoke instabilities in Hall thrusters. IEEE Transactions on Plasma Science, 39(11):2952–2953, 2011.

[35] C.L. Ellison, Y. Raitses, and N.J. Fisch. Cross-field electron transport induced by a rotating spoke in a cylindrical Hall thruster. Physics of Plasmas, 19(1):013503, 2012.

[36] S. Tsikata, N. Lemoine, V. Pisarev, and D.M. Gresillon. Dispersion relations of electron density fluctuations in a Hall thruster plasma, observed by collective light scattering. Physics of Plasmas, 16:033506, 2009.

[37] Y.B. Esipchuk, A.I. Morozov, G.N. Tilinin, and A.V. Trofimov. Plasma oscillations in closed-drift accelerators with an extended acceleration zone. Soviet Physics-Technical Physics, 18:928–932, 1974.

[38] A.A. Litvak, Y. Raitses, and N.J. Fisch. Experimental studies of high-frequency azimuthal waves in Hall thrusters. Physics of Plasmas, 11:1701, 2004.

[39] J.J. Ramos. General expression of the gyroviscous force. Physics of Plasmas, 12(11):112301, 2005.